Accepted Manuscript

Magmatic evolution of the Boku Volcanic Complex, Main Ethiopian Rift

Amdemichael Z. Tadesse, Dereje Ayalew, Raphael Pik, Gezahegn Yirgu, Karen Fontijn

PII: S1464-343X(18)30245-0

DOI: 10.1016/j.jafrearsci.2018.08.003

Reference: AES 3292

To appear in: *Journal of African Earth Sciences*

Received Date: 7 June 2017

Revised Date: 30 July 2018

Accepted Date: 3 August 2018

Please cite this article as: Tadesse, A.Z., Ayalew, D., Pik, R., Yirgu, G., Fontijn, K., Magmatic evolution of the Boku Volcanic Complex, Main Ethiopian Rift, *Journal of African Earth Sciences* (2018), doi: 10.1016/j.jafrearsci.2018.08.003.

MAGMATIC EVOLUTION OF THE BOKU VOLCANIC COMPLEX, MAIN ETHIOPIAN RIFT

Amdemichael Z. Tadesse[1], Dereje Ayalew[1], Raphael Pik[2], Gezahegn Yirgu[1] and Karen Fontijn[3]*

1. *School of Earth Sciences, Addis Ababa University, P.O. Box 1176, Addis Ababa, Ethiopia*
2. *CRPG-CNRS, B.P. 20, 54501 Vandoeuvre-le`s-Nancy Cedex, France*
3. *Department of Earth Sciences, University of Oxford, South Parks Road, Oxford OX13AN, United Kingdom*

Corresponding author (*): amdemichael.zafu@aau.edu.et

MAGMATIC EVOLUTION OF THE BOKU VOLCANIC COMPLEX, MAIN ETHIOPIAN RIFT

Amdemichael Z. Tadesse[1], Dereje Ayalew[1], Raphael Pik[2], Gezahegn Yirgu[1] and Karen Fontijn[3]*

1. *School of Earth Sciences, Addis Ababa University, P.O. Box 1176, Addis Ababa, Ethiopia*
2. *CRPG-CNRS, B.P. 20, 54501 Vandoeuvre-le`s-Nancy Cedex, France*
3. *Department of Earth Sciences, University of Oxford, South Parks Road, Oxford OX13AN, United Kingdom*

Corresponding author (*): amdemichael.zafu@aau.edu.et

Abstract

The Boku volcanic complex is a Quaternary center situated on the axial segment of the Main Ethiopian Rift (MER), located 92 km South-east from Addis Ababa. The main objective of this study is to understand the magmatic evolution of the volcanic complex and to develop a model to answer some outstanding questions related to bimodal products of rift related volcanism, using geological mapping, petrographic and geochemical approaches. The Boku complex is characterized by two main phases of activity: pre-caldera/caldera forming eruptive activity and post-caldera eruptive activity. The volcanic stratigraphy consists from bottom to top of a sequence of rhyolitic lava flows, pumice flows, welded ignimbrite, pumice fall, rhyolitic lava dome, obsidian flow, lower basaltic lava flow, ash flow, basaltic scoria and upper basaltic lava flows. The lithologic varieties together with the geochemical results indicate that the Boku eruptive products are bimodal in composition; no intermediate compositions are found. The mafic rocks are transitional to weakly subalkaline basalts while the silicic rocks are predominantly peralkaline rhyolites. These two groups of rocks are co-genetic and related to each other by fractional crystallization processes starting from mantle-derived basaltic magma with a small component of crustal contamination. The available geophysical, geochemical and field data suggest that the evolution of the evolved silicic center which hosts a bimodal rock distribution can be explained as a result of prolonged stagnation of transitional basaltic melt (sourced from the mantle) at relatively high pressures, where these evolve to intermediate compositions. The transitional basaltic melts can occasionally erupt to the surface along weakness lines such as faults that infrequently cut the

lower part of the shallow reservoir, generating basalts from the intra-caldera and lateral eruptive centers. We consider the intermediate magma is mechanically trapped at mid-crustal depths because of its higher crystal load (ca. 50%). Silicic magma is formed at shallow depth by prolonged fractional crystallization of the intermediate magma and minor assimilation of crustal material. These silicic magmas generate both effusive and explosive eruption products in the overall stratigraphy of the volcanic complex.

Keywords: Boku volcanic complex, Main Ethiopian Rift, eruptive history, petrogenesis, fractional crystallization, Peralkaline rhyolite, Daly gap.

1. Introduction

Continental rift zones are sites of lithospheric stretching, which occurs in response to far-field plate forces such as slab pull, ridge push and tractions at the lithosphere-asthenosphere boundary induced by mantle flow as a result of sinking oceanic plate (Ring, 2014). The extension of the crust is achieved through normal faulting that thins the brittle crust; dense lithospheric mantle rocks rise upward to replace the thinning crust (Buck, 1991; Buck, 2006; Weissel and Karner, 1989; Bastow et al., 2010; Ebinger and Casey, 2001; Casey et al., 2006). The East African Rift System (EARS) can be taken as the model example of a continental rift (Ring, 2014). The EARS is split into Eastern and Western branches. The Eastern branch extends continuously from the Afar of Ethiopia, through central Ethiopia and Kenya to northern Tanzania, and is characterized by an almost continuous chain of volcanoes. The Western branch comprises a series of deep rift basins and distinct volcanic zones, engulfing the Tanzanian craton on its western side, from Lake Albert in Uganda/DRC down to Lake Tanganika and further south to the Malawi Rift (Macgregor, 2015; Morley, 1999).

Previous works (e.g. Ebinger et al., 2000) suggest that the Main Ethiopian Rift (MER) represents the link region between the Afar triple junction and the Turkana rift in Kenya. The MER is divided into three main segments; Northern, Central and Southern MER (Corti, 2009; Mohr, 1983b; Woldegabriel et al., 1990; Hayward and Ebinger, 1996). These segments reflect different stages of the continental extension process that are interpreted from differences in fault architecture, timing of volcanism and deformation, and crustal and lithospheric structure (e.g. Hayward and Ebinger, 1996). The axis of the MER is characterized by the presence of Quaternary central volcanic complexes which include Boku, an inconspicuous and very poorly known caldera with numerous scoria cones. The Boku

Volcanic Complex (BVC) is located in a transitional zone between the Central and Northern MER segments at about 92 km from Addis Ababa and 2 km southeast of Adama (Nazret).

The MER is a fairly extensively studied segment of the EARS. However, many scientific questions remain unsatisfactorily solved, particularly those related to the tectono-magmatic evolution and activity of individual volcanic centers. For instance, after widespread Miocene-Pliocene volcanism, the Quaternary magmatic activity became mostly localized on the rift axis, with products showing a typical bimodal composition (dominantly basaltic and rhyolitic composition). This compositional gap (also known as the Daly gap) remains a poorly understood aspect of the rift-related magmatism, and different petrogenetic models have been proposed. Most authors suggest the peralkaline rhyolites to be derived from their parent basalts by extreme fractional crystallization, whereas others also invoke a component of crustal contamination (e.g. Gasparon et al., 1993; Peccerillo et al., 2003; 2007; Rooney et al., 2007; Trua et al., 1999). In addition to this, there is no full agreement among scholars on the origin of silicic rocks and their relations to mafic rocks (Peccerillo et al., 2007). This study is motivated by the controversy related to the genesis and relationship between the two groups of rocks. Large caldera-forming volcanic complexes in the MER such as Gedemsa, Aluto, Kone and Fanta'Ale have been studied for their eruptive histories and geochemical characteristics (e.g. Ayalew et al., 2016; Fontijn et al., 2018; Giordano et al., 2014; Hutchison et al., 2016; 2018; Rampey et al., 2010) , but others, like Boku, have not been studied in any detail. The main objective of our study is, therefore, to describe its eruptive products and geochemical characteristics for the first time, as well as to better understand the magmatic evolution. A further objective is to develop a model answer for the question of bimodal volcanism in a continental rift setting.

2. Regional Setting

2.1. MER volcanism

The Main Ethiopian Rift (MER) is a key area of the EARS that connects the Red Sea-Gulf of Aden junction (Afar depression) with the Kenya Rift (Turkana depression) (e.g. Corti, 2009; Woldegabriel et al., 1990; Hayward and Ebinger, 1996; Mohr, 1983b; Chorowicz, 2005). The Ethiopian Rift extends for about 1000 km in a NE–SW to N–S direction from the Afar depression southwards to the Turkana depression. It is ~80 km-wide on average and separates the uplifted Ethiopian western and eastern plateaus (Mohr, 1983b). MER extensional deformation started to develop in the late Oligocene-early Miocene (e.g. Ebinger et al., 2000;

Bonini et al., 2005; Wolfenden et al., 2004). GPS kinematic data constrains present-day extension rates to ca. 5 mm/yr (Saria et al., 2014). The adjacent plateaus are mainly made up of Eocene–Late Oligocene igneous rocks related to the Ethiopian-Yemen flood-basalt province (Trap series; Corti, 2009; Rooney, 2017). They are predominantly composed of basalt and intercalated silicic volcanics which have built a sub-aerial volcanic pile, typically 500–1500 m thick and locally attaining 3000 m (Mohr and Zanettin, 1988; Rooney, 2010; Rooney et al., 2014). The total area presently covered by these volcanic rocks has been estimated to 600,000 km^2 (Mohr, 1983a). Immediately after the flood basalt eruptive episode a number of large shield volcanoes developed on the surface of the volcanic plateau from 30 Ma to about 10 Ma (Kieffer et al., 2004; Furman et al., 2006; Rooney et al., 2011).

Magmatic activity in the MER has been episodic rather than continuous (Woldegabriel et al., 1990). After the prevalent Mio-Pliocene volcanism, the Quaternary magmatic activity has been mostly restricted to the rift floor and is partly associated with a NNE-SSW trending *en echelon* fault system (the Wonji Fault Belt). The Quaternary stages of the rift-related volcanism have been marked by eruptions of large amounts of silicic rocks from central volcanoes, basalts predominantly erupted from fissures and scarce intermediate compositions (e.g. Mohr, 1971; Mohr and Zanettin, 1988; Peccerillo et al., 2003; 2007; Fontijn et al., 2018). Such a bimodal distribution of chemical compositions is a common feature of many rift volcanoes, though its origin is still debated (e.g. Rapprich et al., 2016; Giordano et al., 2014; Boccaletti et al., 1995; Chernet and Hart, 1999; Gasparon et al., 1993; Peccerillo et al., 2003; 2007; Ronga et al., 2010; Rooney 2010; Rooney et al., 2011; Rooney et al., 2014; Rooney et al., 2007; Hutchison et al., 2016).

2.2. Geophysical background on the central MER

The thickness of the crust beneath the MER sharply decreases from the plateau to the rift axis. On the western and eastern plateau the crustal thickness is ca. 38-40 km (Mackenzie et al., 2005; Dugda et al., 2005; 2007; Keranen et al., 2009; Keir et al., 2006). Along the rift axis, the crustal thickness varies from 33-35 km in the northern and central MER, to 24-26 km in southern Afar (Dugda et al., 2005; Keir et al., 2006). Few geophysical data are available for the southern sector of the MER. Receiver function analysis from the Ethiopian Broadband Seismic Experiment (Dugda et al., 2005; Maguire et al., 2006) suggest a crustal thickness decrease in the southern MER to values of ~30 km, consistent with gravity modeling (Mahatsente et al., 1999). The majority of the crustal thickness variation is lodged

in the upper crust, whereas the lower crust is considered to have a relatively constant thickness. The overall lithospheric strength generally decreases drastically from the Kenyan to the Ethiopian rift as a result of increasing temperature of the lithosphere (Keranen et al., 2009).

Crustal tomography conveys the existence of elongate bodies along the rift axis of ca. 20 km wide and 50 km long. These anomalous bodies are separated and laterally offset in a right-stepping *en-echelon* manner (and coincide with the magmatic segments situated on the floor of the rift) and characterized by a high Vp/Vs ratio (Daly et al., 2008; Maguire et al., 2006; Keranen et al., 2004) and relative positive Bouguer anomalies (Mahatsente et al., 1999). These bodies are interpreted as cooled mafic intrusions and/or partial melts in the crust and upper mantle (Daly et al., 2008). The presence of melt is further suggested by shear wave velocities indicating high temperatures (Keranen et al., 2009; Keranen et al., 2004).

3. Previous work on Boku Volcanic Complex

Limited knowledge exists on the petrology and geochemistry of BVC. The work by Boccaletti et al. (1999) and a geological map prepared by Damte et al. (1992) are the only works that give some information on the distribution, stratigraphy, and geochemical characteristics of BVC rocks. The 1:50,000 scale geological map of the Nazret-Dera area by Damte et al. (1992) reveals the general lithologic variations, relative timing and distribution of tectonic structures. Boccaletti et al. (1999) established the volcanic stratigraphy of the Nazret-Dera area based on the radiometric dating performed by Bigazzi et al. (1993) and Morton et al. (1979). Accordingly, the Eastern margin unit consists of the older volcanic rocks in the stratigraphy and that have an age of ca. 1.8 Ma. The Eastern margin unit is overlain by Quaternary volcanic products which are associated with the Wonji Fault Belt (Wonji group). Boccaletti et al. (1999) identified seven geological units within the Wonji group and grouped the entire suite of volcanic products from the Boku volcano together as the Boku-Tede Unit (Fig. 4).

4. Materials and Methods

Detailed field investigations of the eruptive products and tectonic structures at the Boku Volcanic Complex were carried out in October 2015 and resulted in a volcanological sketch map of the area. Representative samples were collected for further petrographic and geochemical analysis. Thin sections were prepared at the School of Earth Sciences, Addis

Ababa University. Petrographic studies were performed on a large number of selected samples, covering the variety of lithologies described in the field.

Thirty representative samples were then selected for further geochemical analysis. Clean, non-weathered samples were crushed in a tungsten jaw crusher and powdered using an agate ball mill. Lithic fragments entrained in ignimbrite were manually removed from the crushed samples before proceeding with the next step.

The powdered rock samples were analyzed for major and trace element composition using Inductively Coupled Plasma Optical Emission Spectroscopy (ICP-OES) and ICP-Mass Spectroscopy (ICP-MS) respectively, at the Centre de Recherche Pétrographique et Géochimique (CRPG) of the University of Lorraine, France. Further details on the working procedure of ICP-OES and ICP-MS are given in Fassel and Kniseley (1974) and Montaser (1998) respectively. The reproducibility for the different trace elements is comparable to that presented in other papers using the same facilities and analytical protocols (e.g. Pik et al., 1999).

5. Results

5.1. Eruptive products and petrographic descriptions

The volcanic geology of the BVC comprises a wide range of volcanic products as illustrated in Fig 2. The eruptive units are described according to their stratigraphic succession (presented in the composite stratigraphy; Fig 2c), as deduced from their vertical contact relationships in the field and information from published data. The composite stratigraphy is developed from different outcrops which incorporate more than one eruptive unit. The major eruptive units identified in the area (from the oldest to the youngest) are: a) rhyolitic lava flow, b) pumice fall and flow, c) welded ignimbrite, d) rhyolitic lava dome, e) obsidian flow, f) lower basaltic lava flow, g) ash flow and fall, h) upper basaltic lava and basaltic scoria. Some additional thin eruptive units comprised of pumice and ash falls and flows are not included in the composite stratigraphy. These thin eruptive units are, however, presented in the lithological descriptions below.

a) Rhyolitic lava flow (Qrf)

Rhyolitic lava makes up more than half of the relative thickness in the composite stratigraphy and comprises two of the ten identified major eruptive units. These rhyolitic lavas are

generally grey to pink in colour and occur as lava flows and lava domes. The lowermost rhyolite lava flow in the stratigraphic succession forms a sharp contact with a pumice flow on top. The rock is porphyritic with 16-18% phenocrysts and 94-92% groundmass. The phenocryst is predominantly alkali feldspar (8-9%). The groundmass is microcrystalline and mainly composed of alkali feldspar and quartz. The rhyolite shows flow banding expressed in some exposures as clear white and dark red laminations, with a maximum dip of 40^0. The phenocrysts are oriented along the banding and the unit has a maximum vertical thickness of 45 m.

b) Pumice fall and flow (Qpl and Qpw)

Unconsolidated pyroclastic deposits occur in two varieties: pumice flow and pumice fall. These deposits comprise the products of one eruptive sequence with well preserved crystal-rich pumice clasts. The pumice flow deposits are mainly composed of pumice fragments (with average grain size of 3.5 cm) in a matrix of finer ash and covers a large area relative to the pumice fall deposit (6.9 km^2 of pumice flow and 4.9 km^2 of fall deposit). The pumice lapilli are generally rounded. At different exposures, the pumice flow deposit shows variations in thickness (up to a maximum of 13 m), and poor sorting, with blocks (up to 7 cm diameter) of lithic fragments. The lithic fragments are mainly obsidian and rhyolite lava (Fig 3a). The pumice flow deposit is directly overlain by different eruptive units in different places: pumice fall, rhyolite lava dome or welded ignimbrite. At the southern tip of the Boku ridge (probably representing the remnant of the caldera rim) the pumice flow deposit is intercalated with ash flow units (Fig 3b).

Pumice fall is mainly composed of well-sorted, fine to coarse-grained pumice fragments and is exposed in different parts of the study area. In the field, two different pumice fall layers are observed. The lower pumice fall deposit underlies the rhyolite lava flow and has a maximum thickness of 4 m. The Upper pumice fall layer is observed on top of the rhyolite lava dome and has a maximum thickness of 1 m. This pumice fall deposit in turn is overlain by ash fall and ash flow deposits (Fig 3c). Both the lower and upper pumice fall deposits are well sorted, maintain locally uniform thicknesses, and comprise low-density, grey to yellow-altered, crystal-poor (alkali feldspar) pumice lapilli up to 7 cm in diameter. The upper pumice fall is generally finer grained than the lower one. The deposits are mainly exposed along road cuts and rarely on cliff edges.

c) Welded ignimbrite (Qpw)

A welded ignimbrite unit directly overlies the widespread pumice flow. The rock is grey in color and contains black *fiamme* in some exposures as well as lithic rock fragments. These rock fragments have a grey color and show flow banding, and are interpreted as rhyolite lava. The grey to white matrix of the ignimbrite is mostly fine-grained and porphyritic with white visible crystals. Phenocrysts make up ca. 28% of the rock, and predominantly comprise quartz (17%), alkali feldspar (8%), Fe-Ti oxides (2%) and pyroxenes (1%). The groundmass is microcrystalline and mainly composed of quartz and alkali feldspar. From the modal proportion distribution of the phenocrysts we infer the welded ignimbrite to be rhyolitic in composition.

d) Rhyolitic lava dome (Qrd)

The rhyolitic lava dome represents the greatest thickness in the composite stratigraphy. It occurs as either grey or pink rhyolite and generally has a flat top surface. In the upper part of the Boku section, rhyolite lava material intercalates with poorly welded ash flow deposits and fragmented obsidian. The largest lava dome material at this exposure is approximatly 90 m thick. We interpret the rhyolite to have been dome-forming because of its large height relative to its width, and the appearance of subvertical flow banding. The rock shows a hyalopilitic texture, which is a special type of trachytic texture in which alkali feldspar microlites are oriented parallel and concentric around bigger mineral grains. In thin section the rhyolite shows a porphyritic texture with small volumetric proportions (18% to 23%) of phenocrysts. The phenocrysts comprise upto 13% alkali feldspar, 4-7% Fe-Ti oxides and 4-5% quartz. The groundmass is composed of microcrystalline quartz, alkali feldspar and reddish stains (that might be clay minerals from hydrothermal alteration).

e) Obsidian flow (Qrd)

Obsidian lava flows show a more or less uniform character compared with the other lithologic units found in the area. Two categories are identified based on physical appearance. The first one is massive obsidian and the second variety is fragmented and very fragile. Massive obsidian exposed in the upper part of the stratigraphy, is intercalated with dark grey, aphanitic rhyolite lava. The fragmented obsidian is intercalated with the rhyolite lava dome and minor ash fall deposits.

f) Lower basaltic lava flow (Qbl)

Basaltic lava flows form a gently sloped terrain in the study area and also exposed along fault scarps forming steep cliffs. Based on stratigraphy and petrological characteristics, the basaltic lava flow is classified into two units; lower basalt (Qbl) and upper basalt (Qbu, see section 5.1h). The lower basalt is constituted by a basaltic lava flow underlain by a thin black scoriaceous base. The scoria fragments range in size from lapilli to blocks. The lava flow has a maximum thickness of 13.5 m and underlies an ash flow deposit. The rock is mostly aphanitic but in some areas shows a porphyritic texture. In both cases it is common to observe a dark grey color and polygonal joints on the rock surface. The porphyritic basalt comprises 29-55% of phenocryst. The phenocryst contains 18-24% plagioclase feldspar, up to 15% Fe-Ti oxides, up to 14% olivine, 2% clinopyroxene, 1% orthopyroxene and 1% alkali feldspar. The mineralogical composition of the plagioclase feldspar is labradorite (An_{50-70}) with sporadic bytownite (An_{70-90}). The groundmass is microcrystalline and mainly composed of olivine, plagioclase feldspar and Fe-Ti oxides. This rock unit is exposed only in the southeastern and northwestern part of the volcano.

g) Ash flow and fall (Qra)

Pyroclastic ash flow and fall deposits have the largest coverage in the study area and form gently sloping to flat terrain. These deposits are generally thin and intercalated with other lithologies. Based on their physical characteristics, they are classified into two types: ash flow and ash fall. Matrix-supported ash flow deposits are only represented in one position in the composite stratigraphy (upper ash flow, Qra), but also occur intercalated with the pumice flow deposits (Qpw; Fig 2c). In this lower sequence the ash flow deposits obtain a maximum thickness of 0.7 m, as exposed in Boku section. The upper ash flow (Qra), with a maximum thickness of 12 m, is overlain by the lower basaltic lava flow and thin alluvial sediments in the western part of the study area. Generally the ash flow deposits have a pale yellow color, are moderately welded, poorly sorted, contain lithic fragments and show variations in vertical thickness. The lithic population is mainly composed of basalt, obsidian and rhyolite up to 3 mm size.

Ash fall deposits are the second type of fine-grained pyroclastic deposits found in the volcanic complex. They are not presented in the composite stratigraphy because they are generally thin. They occur intercalated with pumice fall (Qpl) and ash flow (Qra) deposits. The ash fall deposits are pale yellow to grey, well sorted, partially indurated and have a

consistent local thickness, up to a maximum of 1 m (representing a sequence of different volcanic pulses).

h) Upper basaltic lava (Qbu) and Basaltic scoria (Qbs)

The youngest volcanic products found in the Boku volcanic complex are the upper basaltic lava flows (Qbu) and underlying basaltic scoria (Qbs). These two varieties are easly identifiable on a topographic map, as they form cone like structures that are typically characterized by a gentler slope on one side of the cone. The cones themselves are made of scoria while the gentle slope is typically formed by the associated basaltic lava flow. Most cones show an elliptical geometry with their longest axis parallel to the regional tectonic NE-SW direction, suggesting that their eruption is controlled by preexisting structures (e.g. Mazzarini et al., 2016).

Scoria fall deposits are mainly exposed in cliffs and quarries where the materials are excavated as a raw material for cement production and as aggregates for road construction. Deposits are red or black, have amaximum thickness of 40 m, and show rhythmic bedding with blocks and bombs up to 12 cm in diameter.

The basaltic lava flows (Qbu) are up to 2 m thick and are closely associated with the scoria deposits. The basalts are dark-grey, porphyritic and vesicular, with some vesicles filled with secondary minerals. In thin section, they show a seriate texture, with a wide range of phenocryst grain sizes. The phenocryst population is predominantly made up of plagioclase feldspar (31%), with Fe-Ti oxides (up to 12%), olivine (9-12%), clinopyroxene (1-2%), orthopyroxene (1%) and alkali feldspar (1%). The plagioclase feldspar comprises andesine (An_{30-50}) and oligoclase (An_{10-30}), and shows oscillatory zoning. The groundmass is composed of microphenocrysts of the same minerals as the phenocryst population (i.e. predominantly Fe-Ti oxides, plagioclase feldspar, olivine and pyroxenes).

5.2. Correlation and eruptive history of Boku Volcanic Complex

The composite stratigraphy of the BVC is correlated with the regional stratigraphy constructed by Boccaletti et al. (1999) on the basis of our field, petrological and geochemical data (Fig 4). We suggest our rhyolite lava flow, pumice flow, welded ignimbrite, lower pumice fall, rhyolite lava dome and obsidian flow (units Qrf to Qrd) to correlate with the Boku-Tede unit of Boccaletti et al. (1999). The Boku-Tede unit was radiometrically dated

using K-Ar dating at 0.51-0.83 Ma (Boccaletti et al., 1999; Bigazzi et al., 1993; Morton et al., 1979). The products under Boku-Tede are ignimbrite flows, pyroclastic falls, and highly fractured lava domes with associated obsidian layers (Boccaletti et al., 1999). The lower basalt lava flow (Qbl) is correlated with their Bofa unit (0.44-0.61 Ma) which have the characteristics of mafic lava flows with fissural origin; the upper ash flow (Qra) is correlated with the Dera-Sodore unit (Boccaletti et al., 1999). Finally the basaltic scoria and upper basaltic lava flows are correlated with the 0.16-0.23 Ma Melkasa (or Wonji) unit (Damte et al., 1992).

Our composite stratigraphy and correlation with the primary regional units therefore suggest that, pre-caldera activity and caldera-forming eruption(s) at Boku took place between 0.51 and 0.83 Ma. Early products in the BVC stratigraphic sequence were mostly effusive, with the emplacement of rhyolite lava flows. This was followed by a phase of highly explosive activity emplacing widespread pumice fall and flow deposits, as well as welded ignimbrites, which were possibly associated with the formation of the caldera. The earliest post-caldera or latest syn-caldera volcanism, as exposed mainly in the caldera walls, was again effusive, in the form of rhyolite lava domes. The post caldera eruptive activity at Boku resulted in the emplacement of the lower basaltic lava flows (at 0.44-0.61 Ma), upper ash flow and finally basaltic scoria and associated lava flows (since 0.23 Ma).

5.3. Geochemistry

Major and trace element data were obtained on a representative selection of all major stratigraphic units to understand the magmatic evolution of the BVC; these data are reported in Table 1. Loss of Ignition (LOI) is generally low (<2.5 wt%) except for some pumice samples, where we find LOI values up to 9 wt% (Table 1). These samples also show low Na_2O values relative to the rhyolite lava samples, and so the high LOI values are attributed to post-depositional alteration and the mobile element data on these samples are to be treated with caution (Peccerillo et al., 2003; Fontijn et al., 2013). In addition to the new geochemical results, published data from previous works (Rapprich et al., 2016; Giordano et al., 2014; Boccaletti et al., 1995; Chernet and Hart, 1999; Gasparon et al., 1993; Peccerillo et al., 2003; 2007; Ronga et al., 2010; Rooney 2010; Rooney et al., 2011; Rooney et al., 2014; Rooney et al., 2007; Hutchison et al., 2016) were used for comparison and are shown as grey fields and point data in the geochemical diagrams (Fig 5-10).

372 5.3.1. **Major element geochemistry**

373 The samples show a typical bimodal composition on the Total Alkali-Silica classification
374 diagram (after Le Bas et al., 1986, see Fig 5). The distribution of the samples mainly falls on
375 the subalkaline-alkaline divide, with a felsic field with SiO_2 above 68 wt% and a mafic field
376 with 45 to 50 wt% SiO_2. The MgO content of the mafic series ranges from 5.79 to 9.02 wt%.
377 Nearly all felsic samples are rhyolitic in composition, with two samples near the trachyte-
378 trachydacite field. All the mafic samples are basaltic in composition and fall within the
379 transitional to subalkaline field (Fig 5). CIPW norm calculations suggests the basaltic
380 samples to be olivine-normative (14-24%; nepheline <2%) transitional to weakly subalkaline
381 basalts (Table 1).
382
383 The plot of agpaitic index against SiO_2 (Fig 6a) shows that the silicic volcanic products
384 classify as peralkaline rhyolites, except for one pumice sample that has an agpaitic index
385 value of 0.81 and falls in the subalkaline field. The peralkaline rhyolites with low LOI values
386 indeed have acmite (Ac) in their norm, consistent with their high agpaitic index (Table 1).
387
388 The silicic rocks are further classified on the diagram of Al_2O_3 against FeO_t after Macdonald
389 (1974). The peralkaline rhyolites are reclassified into comendite (three samples) and
390 pantellerite (the rest of samples; Fig 6b). One sample that was classified as subalkaline based
391 on its agpaitic index (Fig 6a) here classifies as comenditic trachyte.
392
393 The Harker variation plots are shown in Fig 7 for selected major oxides. These follow the
394 trends seen at other volcanoes in Ethiopia: positive correlations of TiO_2, Al_2O_3, FeO_t, CaO,
395 and P_2O_5 with MgO and negative correlations of Na_2O, K_2O and SiO_2 against MgO (except
396 for the altered pumice samples which have lower values of Na_2O, Fig 7f). In addition to the
397 general trend within similar types of rock (i.e basalt and rhyolite composition) a well-defined
398 variation trend is shown on the selected major element plots against MgO (Fig 7). The
399 observed variation in the major element for the mafic and felsic rocks consistently shows
400 their difference in the evolution stage. The mafic rocks generally exhibit high contents of
401 TiO_2, Al_2O_3, FeO_t, MgO, CaO, P_2O_5 and lower content of Na_2O, K_2O and SiO_2 than the felsic
402 rocks.
403

5.3.2. **Trace element geochemistry**

The BVC rocks display a wide range of trace element concentration. Fig 8 shows the variations between selected trace elements and SiO_2. The compatible trace elements, e.g. Cr, Sc and Sr, show negative correlations. The incompatible trace elements (e.g. Nb, Zn, Rb, Y and Zr) show strong positive correlations against SiO_2. Ba displays incompatible behavior in the mafic samples and compatible behavior in the silicic samples.

Zr displays strong incompatible behavior, with concentrations reaching up to the order of 1000 ppm in the most silicic samples. Zr can therefore be used as a differentiation index. The incompatible trace elements (e.g. Nb) indeed show a positive correlation with Zr and confirm that the silicic rocks have a similar evolution history. It is particularly noticeable that the gap between mafic and silicic samples is narrower when trace elements are plotted against Zr than against SiO_2 (Fig 9). The diagrams (especially Zr against La, U and Rb) strikingly show dispersion on the felsic samples which misfit the fractionation trend in the magma evolution. This dispersal in the incompatible elements can be explained by the interaction of the source magma with crustal material. The enriched value in the ratio of mobile to refractory trace elements in felsic rocks (eg., Rb/Nb:0.8-2.8; Th/Ta:1.5-3.8 and Ba/Nb:0.3-15) also further suggest a possible influence of crustal material in the magmatic evolution history of the BVC.

Rare Earth Element (REE) variations are plotted for a selection of mafic and silicic volcanic products (Fig 10a) normalized to chondrite values (after Boynton, 1984). The enrichment of the Light REE (LREE) in mafic rocks, expressed in terms of $(La/Yb)_N$, ranges between 4.9-6.4. The gentle slope in Heavy REE (HREE) implies the source for the mafic rocks is garnet-free. The pattern of the REE diagram is parallel for all samples. This indicates their derivation from a similar source, with systematic accumulation or removal of mineral phases. The Eu concentration of mafic lavas shows no clear anomaly (Eu/Eu*~1.1) which likely represents no accumulation or fractionation of plagioclase feldspar in the initial stage. The enrichment of LREE ranges expressed in terms of $(La/Yb)_N$. The value ranges between 4.1-8.7 for the silicic rocks. Similar to mafic samples the silicic samples show parallel patterns in the REE diagram. All silicic samples show a negative Eu anomaly (Eu/Eu*<1), which is typically an indication for the fractionation of plagioclase feldspar.

The multi-element spider diagram is shown in Fig 10b normalized to primordial mantle values (McDonough and Sun, 1995). The diagram for the mafic rocks exhibits a bell-shaped

pattern. The diagram further shows a positive anomaly of Ba and a negative anomaly of K relative to the neighboring trace elements like Nb and La. The combination of minor enrichment in Ba and troughs in Nb and La may indicate crustal contamination of the mafic lava during the fractionation process. Overall enrichement in the incompatible elements is consistent with fractionation of different mineral phases, especially plagioclase feldspar. The spidergram for the silicic volcanic product shows troughs in Ba, Sr and Ti. Conversely, the mafic volcanic products have a positive spike in Ba and flatter trends in Sr and Ti. The negative anomalies and flat trend in Ba and Sr respectively for the two groups of rocks are indicative of the late crystallization of alkali and plagioclase feldspar. The Ti troughs for the silicic rocks indicate the removal of accessory ilmenite. Both the mafic and silicic samples generally exhibit less pronounced positive anomalies in Nb, Th, Pb, K and Ce, and negative anomalies in U.

6. Discussion

6.1. Crustal contamination

Before discussing the petrogenesis of the Boku peralkaline rhyolitic rocks it is essential to assess the degree of crustal contamination. From the different diagrams discussed above we can infer that crustal contamination plays a small role in the compositional evolution of the magmas.

Besides the ratio of mobile to refractory trace elements (discussed in section 5.3.2) crustal material involvement is mainly evaluated using the contamination index (La/Nb) and Nb and Ta patterns in the spidergram (Hofmann, 2003; Ayalew and Gibson, 2009; Rudnick and Gao, 2003). Some Boku samples show La/Nb ratios above 1, with a maximum value of 1.24 which may indicate slight contamination by crustal material. The diagrams of La/Nb and Th/Ta against SiO_2 show a slight sub-horizontal to inclined trend (Fig 11a and b) further suggesting minor contamination. The high value of Th/Nb (0.1-0.3) further traces the involvement of crustal material. Crustal contamination has also been suggested in the wider region using trace element and isotope geochemistry (e.g. Gedemsa, Fanta'Ale, Boset and Aluto; Giordano et al., 2014; Ronga et al., 2010; Hutchison et al., 2016; 2018). Compared to Fanta'Ale and Gedemsa (Giordano et al., 2014) the La/Nb and Th/Ta values indicate a slight increment in the case of BVC (Fig 11a and b). This further substantiates the existence of crustal contamination in BVC samples and suggests that the degree of contamination is slightly higher than in the two other volcanoes. Some BVC silicic rocks show low Nb

concentrations down to 42 ppm (Table 1). One sample from the mafic rocks shows lower values of Ce/Pb (10) and Nb/U (30) compared to average MORB and IOB values (Ce/Pb= 25±5; Nb/U=47±10; Hofmann et al., 1986) which further suggest a small involvement of crustal material.

6.2. Petrogenesis of silicic rocks

Some of the outstanding questions related to peralkaline volcanism relate to the origin of peralkaline silicic rocks, their relationship with basaltic magmas, and the reasons for the paucity of intermediate compositions in the eruptive volcanic products. The data presented in this study reveal, in agreement with previous studies, that the Quaternary volcanism in the MER is dominated by a bimodal association of mafic and silicic products, with scarce or no intermediate rocks. This bimodality is also seen at Fanta'Ale and Gedemsa (e.g. Peccerillo et al., 2003; 2007; Giordano et al., 2014) and only small proportions of intermediate rocks are observed at Boset-Bericha and Aluto (e.g. Macdonald et al., 2012; Ronga et al., 2010; Hutchison et al., 2016; 2018; Siegburg et al., 2018).

The observation that the REE diagram is flatter in the heavy REE region (Tb_n/Yb_n=0.34-0.37 and nearly constant Y and Yb concentration), in combination with low CaO/Al_2O_3 (0.6-0.8) and Zr/Y ratios (5-14), suggests that the source of the mafic rocks is garnet-free. The mafic samples exhibit the following compositional ranges: MgO (5.79-9.77 wt%), Cr (158-581 ppm) and Ni (31-154 ppm); and are therefore more evolved than primary MORB magmas (after Frey et al., 1978; Baker et al., 1996; Kushiro, 1996; Allègre et al., 1977). From this we infer that the mafic rocks at BVC have undergone moderate fractionation of olivine and clinopyroxene (suggested from solidification indices and Mg# <50). The Ba/Nb ratio ranges 10 to 22.8 with an average value of 16.4. This value is higher than the average value for primitive mantle (after McDonough and Sun, 1995), and this can be attributed to contamination by continental crust (Ba/Nb=57; Rudnick and Gao, 2003) and/or fractionation processes.

The major and trace element compositions are used to evaluate whether the mafic and silicic rocks are genetically related or not. The Harker diagrams have two clusters of sample distribution separated by a wide compositional gap commonly referred to as the Daly gap (e.g. Bunsen, 1851; Daly, 1925; Peccerillo et al., 2003; Macdonald et al., 2008; Ferla and

Meli, 2006; Lowenstern et al., 2006). The presence of this compositional gap does however not preclude the genetic association of the rocks. The gap significantly narrows when highly incompatible trace elements are considered as a differentiation index. This is illustrated in Fig 9 where selected trace elements are plotted against Zr. These plots show positive correlations with slopes of approximately 1. Such a relationship is commonly interpreted as indicative of the genetic relationship or co-genetic nature of the mafic and silicic rocks (e.g. Hutchison et al., 2016). Apart from using elemental concentrations to determine the source resemblance of the volcanic suites, the systematic behavior of some highly incompatible element ratios like Nb/Ta, Zr/Hf and Ce/Pb are strong indicators of the co-genetic nature of the magmas. These ratios do not change significantly in lavas from the same source. The highly incompatible element ratios like Nb/Ta (11-14), Zr/Hf (35-42) and Ce/Pb(7-14) show a narrow range which can determine the genetic relationships of the mafic and felsic suits. This is further supported in spidergrams and multi-element variation diagrams in which mafic and silicic rocks of selected samples show parallel patterns, exhibited by a marked LREE enrichment relative to HREE, like also seen at other volcanoes in the MER (Ayalew and Gibson, 2009; Ronga et al., 2010; Trua et al., 1999). This result can be substantiated by further analysis of isotope (especially Sr and Nd isotopes).

Several hypotheses have been proposed to explain the genesis of peralkaline volcanism in the Ethiopian rift (Trua et al., 1999; Peccerillo et al., 2007). The first one is partial melting of the old continental crust (crustal anatexis) and basalt (e.g. Thy et al., 1990; Hay and Wendlandt, 1995; Beard and Lofgre, 1991). The second mechanism is a two-step of process; partial melting followed by fractional crystallization (e.g. Trua et al., 1999; Bohrson and Reid, 1997); the third is fractional crystallization with little involvement of crustal material (e.g. Peccerillo et al., 2003; Giordano et al., 2014; Hutchison et al., 2016). Crustal anatexis alone cannot explain the petrogenesis of the peralkaline volcanic products (Peccerillo et al., 2003). The geochemical composition of Ethiopian Precambrian rocks that constitute the basement is compared with our data of BVC samples. If crustal anatexis played a significant role, melting processes (i.e. partial melting) would be expected to drive up the ratios of incompatible elements (e.g. Rb/Nb and Rb/Zr) in the melt (BVC in this case) relative to the source (Precambrian rock), which is not the case in our sample set (Table 2). Crustal anatexis is therefore unlikely to play a significant role in the formation of peralkaline rocks of Boku. The incompatible element ratios of BVC rocks are also very low when compared to the flood

basalts (e.g. Kieffer et al., 2004). This indicates that partial melting of the Ethiopian flood basalt cannot explain the petrogenesis of Boku volcanic products either.

6.3. Fractional crystallization

Our major and trace element data are consistent with a fractional crystallization trend that is dominated by the removal of different mineral phases at different stages of the fractionation. The sharp, steep positive correlations of FeO_t and MgO are attributed to the crystallization of ferromagnesian mineral phases (olivine and pyroxenes). Another phase that fractionates from the system is plagioclase feldspar, as indicated by the decrease of CaO, Al_2O_3 and Sr. Ilmenite and apatite are also interpreted to fractionate from the system based on the decrease in TiO_2 and P_2O_5. Finally, late-stage alkali feldspar fractionation is suggested by the negative correlations of K_2O, Na_2O and Ba in the high-SiO_2 compositions. The dominance of alkali feldspar fractionation in highly evolved rhyolite is further supported by the field description and petrographic observations on thin sections. The role of the fractionation process is significantly visible within the silicic and basaltic groups of rocks (Fig 7). In terms volatile exsolution from the magma, fractionation plays a significant role in the magmatic history of BVC. This process increases the explosively of the magma which is clearly visible in the pre to syn eruptive sequence of BVC.

Both batch and partial melting processes are able to generate liquids with variable enrichments in incompatible elements, but with moderate depletion in compatible elements. In contrast, fractional crystallization is much more efficient in producing compatible element depletion than incompatible element enrichment (Ayalew et al., 2002; Ayalew and Gibson, 2009; Peccerillo et al., 2003). Therefore, models of incompatible against compatible trace elements are potentially powerful tools to further discriminate between fractional crystallization and partial melting processes. Sr against Rb is plotted for this purpose (Fig 12a). The plot shows strong variations in compatible element concentrations (Sr) and only limited variations in incompatible element concentrations (Rb), suggesting that fractional crystallization is the dominant process in the magmatic differentiation of BVC rocks.

6.4. Petrogenetic modeling

In this section the evolution of BVC silicic magmas is modeled. The parent magma selected is sample NB-01, one of the least differentiated in our suite of samples (MgO 8.81 wt%; Ni 88 ppm). The partition coefficients selected for the model are 4.7 for Sr and 0.029 for Rb

(Ewart and Griffin, 1994). A model of fractional crystallization has been tested by following Rayleigh's law from the least differentiated basalt sample using the equation (after Neuman et al., 1954):

$C^i_L = C^i_o F^{(Di-1)}$; where C^i_L: concentration of trace element i in the liquid

C^i_o: concentration of trace element i in the parent magma

F: weight proportion of liquid

D^i: bulk distribution coefficient for element i.

By applying the above equation we calculate the degree of fractionation and the concentrations of the daughter liquid. To generate the silicic BVC compositions, the mafic magma needs at least a degree of fractional crystallization of 80% (Fig 12b). At this degree of fractionation the composition of the calculated liquids is very similar to that of the analyzed liquid for all trace elements, except for Pb and Sr (Fig 12c and d). The resulting data can be explained by the fractionation process occurring in open system and allowing interaction of the magma with the surrounding crustal material.

Rhyolite-MELTs software (after Gualda et al., 2012) is applied to further understand the crystallization sequence of the highly evolved magma from their parent basaltic magmas. The simulation is applied at different pressure conditions (0.3 kbar to 2 kbar). The process of crystallization was checked against various buffer systems and it was found that the QFM buffer system produces peralkaline magma. The crystallization series for different pressure conditions shows that the silica content increases from low to medium pressure (0.6 kbar) and starts to decline at higher pressure. The graphs (Fig 13a) show the typical pressure conditions that can be applied to the formation of peralkaline magma; 0.5, 0.6 and 0.7 kbar. The fractionation and ponding of magma at shallow crustal level is consistent with results of geochemical and geophysical studies of Gedemsa volcano and the MER rift axis volcanic centers (e.g. Peccerillo et al., 2003; Rooney et al., 2011; Keranen et al., 2009; Keranen et al., 2004). At these shallow pressure conditions the degree of fractionation is very similar to that constrained by our trace element modeling (F=88 to 90%). Under pressure conditions which can produce peralkaline magma, first the basaltic magmas fractionate to intermediate compositions and then progressively produce peralkaline magma (Fig 13b). Our Rhyolite-MELTs modeling at low pressure (e.g. 0.6 kbar) indicates that the first phase to crystallize and fractionate from the primitive basaltic melt is olivine at 1141±30 ^{o}C (Fig 13c). Olivine

fractionation is then followed by plagioclase feldspar, clinopyroxene and spinel crystallizing at a temperature of 1091±40 ^{o}C in different proportions. Orthopyroxene and apatite follow at 991±30 ^{o}C and finally Fe-Ti oxides start crystallizing at a temperature of 941±35 ^{o}C. The crystallization of different mineral phases ends at 841±40 ^{o}C.

The proportions of fractionating mineral phases are constrained by mass balance calculation following the methods of Stormer and Nicholls (1978). The chemical composition of each mineral phase is adopted from Boccaletti et al. (1999) who analyzed samples collected in the study area. The validity of the model was confirmed by the r-squared (r^2) value. The mass balance modeling is tested in different ways by considering either fractional crystallization or fractional crystallization with involvement of crustal material. The average upper crust composition (after Taylor and McLennan, 1985) and the Ethiopian basement rocks composition (adopted from Alene et al., 2000; Teklay et al., 1998; Asrat and Barbey, 2003) are considered for the crustal contaminant composition by the optimization technique in the OPTIMASBA modeling workbook (Cabero et al., 2012). To obtain the least differentiated rhyolitic material in the Boku sample set (i.e. sample NB-22; Table 1) with no involvement of crustal material, the primitive basalt fractionates the following minerals: 21% olivine, 14% clinopyroxene, 56% plagioclase feldspar, 8% Fe-Ti oxides and minor apatite (~1%). The Σr^2 is 0.97 in this case. The best fit regression coefficient becomes even better (Σr^2=0.99) when crustal contamination with 0.1 relative ratio of assimilated to crystallized material is considered in the modeling. The proportions of the fractionating minerals (26% olivine, 14% clinopyroxene, 65% plagioclase feldspar, 8% Fe-Ti oxides and minor apatite ~1%).) show a significant change compared to the first model. The most differentiated peralkaline rhyolite (i.e. NB-14; Table 1) is further derived from the least differentiated rhyolite by alkali feldspar and quartz fractionation.

Our major and trace element modeling suggests there is formation of intermediate magma composition. Field observations around Boku volcano and most other MER volcanic centers; however, shows scarce occurrences of intermediate erupted magmas. Therefore, the rare occurrences of intermediate magmas may possibly be related to their non-eruption (e.g. Macdonald 2012; Ronga et al., 2010). Small proportions of intermediate magma formation have been ascribed to a sudden drop followed by a rapid increase in oxygen fugacity during the crystallization of Fe–Ti oxides near the transition to peralkalinity (eg. Barberi et al.,

1975). This hypothesis is not verified by our major element modeling. The Boku least evolved trachyte-trachydacite compositions are peralkaline already and the Fe-Ti oxides are started to crystallize only after the intermediate magmas have been formed (at 941±35 ^{o}C). Physical controls such as density and/or viscosity can inhibit the ascent of magmas with specific compositions (e.g. Baker et al., 1977; Jones 1979). At centers where intermediate magmas are found (e.g. Boset); these tend to contain high proportions of crystals (eg. Peccerillo et al., 2003; Ronga et al., 2010). The non-eruption of similar intermediate magmas at centers like Boku is therefore possibly related to the high effective viscosities resulting from the high crystal load, in combination with higher densities of magmas. Some experimental and modeling studies (e.g. Marsh 1981; Dufek and Bachmann, 2010; Bonnefoi et al., 1995; Brophy 1991) indeed suggest mechanical trapping of melt by a high crystal load. Melts in these models can only be extracted from the mixture composition after critical crystallization (40-50 vol% crystals). This critical crystal fractionation can change the composition of the mixed magma to silicic and facilitate the melt extraction. Silicic rhyolite melt would generate magmas with even higher viscosities, but also a lower density, facilitating their extraction (e.g. 2400-2600 kg/m^3 for intermediate and <2400 kg/m^3 for silicic melts; Peccerillo et al., 2003). This density difference and generally higher volatile contents (resulting from fractional crystallization) of the silicic magmas may further help to drive them to the surface.

By taking into account the existing geochemical, geophysical and field observation data we can explain the evolution of silicic centers in the MER which comprise mafic and silicic, but scarce or no intermediate volcanic products (Fig 13d). The transitional basaltic melts sourced from upper mantle stagnate at relatively deep level (Bastow et al., 2010; Daly et al., 2008; Maguire et al., 2006; Keranen et al., 2004; Mahatsente et al., 1999) and evolves to intermediate magma compositions. Sometimes the transitional basaltic melt may erupt directly to the surface along structural weaknesses such as faults that infrequently cut the lower parts of the shallow magma reservoirs, and generate basaltic lava flows and scoria cones from intra-caldera and lateral centers (e.g. Peccerillo et al., 2007; Mazzarini et al., 2016). The mush of the intermediate magma has a higher opportunity for mechanical trapping at intermediate depth because of its high crystal load of ca. 50%. Silicic magma will be formed at shallow depths by prolonged fractional crystallization and minor assimilation of the intermediate magma. The variable amounts of volatiles in the silicic melts sometimes

produce explosive eruptions and resulting pyroclastic deposits, alongside obsidian flows and domes in the stratigraphic sequence.

7. Conclusions

A combination of field mapping, petrography and geochemistry provides new perceptions about the eruptive history and magmatic evolution of the Boku volcanic complex and the adjacent silicic centers in the Main Ethiopian Rift. The main conclusions of this study are:

1. The Boku volcanic complex is composed of volcanic products sourced from two main episodes of volcanic activity: Boku pre-caldera/caldera forming eruptive activity and post-caldera eruptive activity. The Boku pre-caldera/caldera forming activity was initially predominantly effusive, then culminated in an explosive phase and finally became non-explosive again. This eruptive activity took place between 0.51-0.83 Ma. The main volcanic products are rhyolitic lava flow, pumice flow, welded ignimbrite, pumice fall, and rhyolitic lava dome and obsidian flow. The post-caldera volcanic activity occurred between 0.16-0.23 Ma. This activity resulted mainly in ash flows, basaltic scoria and basaltic lava flows.

2. The petrographic observations and major element geochemistry reveals that the BVC rocks are bimodal, i.e. predominantly basaltic and rhyolitic, with no intermediate compositions found. The basalts are transitional to weakly subalkaline while the silicic rocks are predominantly peralkaline rhyolite.

3. The major and trace element geochemistry strongly suggests that the basalts and peralkaline rhyolites are genetically related. Major and trace element variations and modeling imply that the rocks are linked by fractional crystallization processes with minor to no crustal contamination. In order to form Boku peralkaline rocks, the parental basaltic magma needs to have undergone at least 80% fractional crystallization.

4. The available geophysical, geochemical and field data suggest that the bimodal rock distribution of the Boku Volcanic Centre can be explained as a result of prolonged stagnation of transitional basaltic melt (sourced from the mantle) at relatively high depth, which evolves to intermediate magma compositions. Occasionally the transitional basaltic melt erupts to the surface along structural weaknesses, to produce basaltic eruptive products from intra-caldera and lateral vents. The intermediate magma possibly be

trapped mechanically at intermediate depth because of its high crystal load. Silicic magma can finally be formed at shallow depth by prolonged fractional crystallization and minor assimilation of the intermediate magma, and produce explosive as well as effusive eruptions.

Acknowledgments

This research was part of the first author's MSc. thesis work. Financial support was provided by a studentship at the School of Earth Science, Addis Ababa University and a research project grant funded by European Research Council and Deep Carbon Observatory (grant number 267255). Karen Fontijn is supported by the UK's Natural Environment Research Council grant NE/L013932/1 (RiftVolc). Different individuals helped by assisting the field work, thin section sample preparation and providing wealthy information about the subject of study; they are Mr. Bahru Zinaye, Mr. Samuel Getachew, Mr. Million Alemayehu and Mr. Wondwossen Sisay. We thank Dr. Mulugeta Alene, Prof. Tanya Furman and one anonymous reviewer for expert reviews that have greatly improved the paper. Dr. Read Mapeo is highly acknowledged for editorial handling.

738 **Reference**

739 Alene, M., Ruffini, R., and Sacchi, R. (2000). Geochemistry and geotectonic setting of
740 Neoproterozoic rocks from northern Ethiopia (Arabian-Nubian Shield). *Gondwana*
741 *Research*, **3**(3):333-347.

742 Allègre, C. J., Treuil, M., Minster, J. F., Minster, B., and Albarède, F. (1977). Systematic use
743 of trace element in igneous process. *Contributions to Mineralogy and*
744 *Petrology*, **60**(1):57-75.

745 Asrat, A., and Barbey, P. (2003). Petrology, geochronology and Sr–Nd isotopic geochemistry
746 of the Konso pluton, south-western Ethiopia: implications for transition from
747 convergence to extension in the Mozambique Belt. *International Journal of Earth*
748 *Sciences*, **92**(6):873-890.

749 Ayalew, D., Barbey, P., Marty, B., Reisberg, L., Yirgu, G., and Pik, R. (2002). Source,
750 genesis, and timing of giant ignimbrite deposits associated with Ethiopian continental
751 flood basalts. *Geochimica et Cosmochimica Acta*, **66**(8):1429-1448.

752 Ayalew, D., and Gibson, S. A. (2009). Head-to-tail transition of the Afar mantle plume:
753 Geochemical evidence from a Miocene bimodal basalt–rhyolite succession in the
754 Ethiopian Large Igneous Province. *Lithos*, **112**(3):461-476.

755 Ayalew, D., Jung, S., Romer, R. L., Kersten, F., Pfänder, J. A., and Garbe-Schönberg, D.
756 (2016). Petrogenesis and origin of modern Ethiopian rift basalts: Constraints from
757 isotope and trace element geochemistry. *Lithos*, **258***:*1-14.

758 Baker, B. H., Goles, G. G., Leeman, W. P., and Lindstrom, M. M. (1977). Geochemistry and
759 petrogenesis of a basalt-benmoreite-trachyte suite from the southern part of the
760 Gregory Rift, Kenya. *Contributions to Mineralogy and Petrology*, **64**(3):303-332.

761 Baker, J., Snee, L., and Menzies, M. (1996). A brief Oligocene period of flood volcanism in
762 Yemen: implications for the duration and rate of continental flood volcanism at the
763 Afro-Arabian triple junction. *Earth and Planetary Science Letters*, **138**(1-4):39-55.

764 Barberi, F., Ferrara, G., Santacroce, R., Treuil, M., and Varet, J. (1975). A transitional basalt-
765 pantellerite sequence of fractional crystallization, the Boina Centre (Afar Rift,
766 Ethiopia). *Journal of Petrology*, **16**(1):22-56.

767 Bastow, I. D., Pilidou, S., Kendall, J. M., and Stuart, G. W. (2010). Melt-induced seismic
768 anisotropy and magma assisted rifting in Ethiopia: Evidence from surface
769 waves. *Geochemistry, Geophysics, Geosystems*, **11**(6).

770 Beard, J. S., and Lofgren, G. E. (1991). Dehydration melting and water-saturated melting of
771 basaltic and andesitic greenstones and amphibolites at 1, 3, and 6. 9 kb. *Journal of*
772 *Petrology*, **32**(2):365-401.
773 Bigazzi, B., Bonadonna, F., Di Paola, G., and Giuliani, A. (1993). K-Ar and fission track
774 ages of the last volcano tectonic phase in the Ethiopian Rift Valley (Tullu Moye area).
775 *Geology and mineral resources of Somalia and surrounding regions. Istituto*
776 *Agronomico Oltremare, Firenze, Relazioni Monografie*, **113:**311-322.
777 Boccaletti, M., Assefa, G., Mazzuoli, R., Tortorici, L., and Trua, T. (1995). Chemical
778 variations in a bimodal magma system: the Plio-Quaternary volcanism in the Dera
779 Nazret area (Main Ethiopian Rift, Ethiopia). *Africa Geoscience Review*, **2**(1):37-60.
780 Boccaletti, M., Mazzuoli, R., Bonini, M., Trua, T., and Abebe, B. (1999). Plio-Quaternary
781 volcanotectonic activity in the northern sector of the Main Ethiopian Rift:
782 relationships with oblique rifting. *Journal of African Earth Sciences*, **29**(4):679-698.
783 Bohrson, W. A., and Reid, M. R. (1997). Genesis of silicic peralkaline volcanic rocks in an
784 ocean island setting by crustal melting and open-system processes: Socorro Island,
785 Mexico. *Journal of Petrology*, **38**(9):1137-1166.
786 Bonnefoi, C. C., Provost, A., and Albarede, F. (1995). The'Daly gap'as a magmatic
787 catastrophe. *Nature*, **378**(6554):270.
788 Bonini, M., Corti, G., Innocenti, F., Manetti, P., Mazzarini, F., Abebe T., and Pecskay, Z.
789 (2005). Evolution of the Main Ethiopian Rift in the frame of Afar and Kenya rifts
790 propagation. *Tectonics*, **24**(1).
791 Boynton, W. (1984). *Cosmochemistry of the rare earth elements.* Elsevier.
792 Brophy, J. G. (1991). Composition gaps, critical crystallinity, and fractional crystallization in
793 orogenic (calc-alkaline) magmatic systems. *Contributions to Mineralogy and*
794 *Petrology*, **109**(2):173-182.
795 Buck, W.R. (1991). Modes of continental lithospheric extension. *Journal of Geophysical*
796 *Research: Solid Earth*, **96**(B12):20161-20178.
797 Buck, W.R., 2006. The role of magma in the development of the Afro-Arabian rift
798 system. In: Yirgu, G., Ebinger, C., Maguire, P. (Eds.), The Afar Volcanic Province
799 within the East African Rift System. Special Publication of the Geological Society,
800 London, pp. 43–54.
801 Bunsen, R. (1851). Ueber die Processe der vulkanischen Gesteinsbildungen Islands. *Annalen*
802 *der Physik*, **159**(6):197-272.

Cabero, M. T., Mecoleta, S., and López-Moro, F. J. (2012). OPTIMASBA: A Microsoft Excel workbook to optimise the mass-balance modelling applied to magmatic differentiation processes and subsolidus overprints. *Computers & geosciences*, **42**:206-211.

Casey, M., Ebinger, C., Keir, D., Gloaguen, R., and Mohamed, F. (2006). Strain accommodation in transitional rifts: extension by magma intrusion and faulting in Ethiopian rift magmatic segments. *Geological Society, London, Special Publications*, **259**(1):143-163.

Chernet, T. (1995). Petrological, geochemical and geochronological investigation of volcanism in the Northern Main Ethiopian Rift-Southern Afar transition region. Unpublished Phd. Thesis, Miami University, Ohio, USA.

Chernet, T., and Hart, W. K. (1999). Petrology and geochemistry of volcanism in the northern Main Ethiopian Rift-southern Afar transition region. *Acta Vulcanologica*, **11**:21-42.

Chorowicz, J. (2005). The east African rift system. *Journal of African Earth Sciences*, **43**(1):379-410.

Corti, G. (2009). Continental rift evolution: from rift initiation to incipient break-up in the Main Ethiopian Rift, East Africa. *Earth-Science Reviews*, **96**(1):1-53.

Cross, C. W., Iddings, J. P., Pirsson, L. V., and Washington, H. S. (1903). *Quantitative classification of igneous rocks*, Univ. Chicago Press.

Daly, R. A. (1925). The geology of Ascension island. In *Proceedings of the American Academy of Arts and Sciences*. American Academy of Arts and Sciences, **60**(1):3-80.

Daly, E., Keir, D., Ebinger, C., Stuart, G., Bastow, I., and Ayele, A. (2008). Crustal tomographic imaging of a transitional continental rift: the Ethiopian rift. *Geophysical Journal International*, **172**(3):1033-1048.

Damte, A., Boccaletti M., Mazzuoli R, Assefa, G., and Tortorici L. (1992). Geological map of the Nazareth Dera Region (Main Ethiopian Rift). Scale 1:50,000. S.E.L.C.A., Florence, Italy.

Dugda, M., Nyblade, A., and Julia, J. (2007). Thin lithosphere beneath the Ethiopian Plateau revealed by a joint inversion of Rayleigh wave group velocities and receiver functions. *Journal of Geophysical Research: Solid Earth, (1978–2012)* **112**(B8).

Dugda, M., Nyblade, A., Julia, J., Langston, C., Ammon, C., and Simiyu, S. (2005). Crustal structure in Ethiopia and Kenya from receiver function analysis: implications for rift

development in eastern Africa. *Journal of Geophysical Research: Solid Earth, (1978–2012)* **110**(B1).

Dufek, J., and Bachmann, O. (2010). Quantum magmatism: Magmatic compositional gaps generated by melt-crystal dynamics. *Geology*, **38**(8):687-690.

Ebinger, C. J., and Casey, M. (2001). Continental breakup in magmatic provinces: An Ethiopian example. *Geology*, **29**(6):527-530.

Ebinger, C., Yemane, T., Harding, D., Tesfaye, S., Kelley, S., and Rex, D. (2000). Rift deflection, migration, and propagation: linkage of the Ethiopian and Eastern rifts, Africa. *Geological Society of America Bulletin,* **112**(2):163-176.

Ewart, A., and Griffin, W. (1994). Application of proton-microprobe data to trace-element partitioning in volcanic rocks. *Chemical Geology,* **117**(1):251-284.

Fassel, V.A., and Kniseley, R. N. (1974). Inductively coupled plasma. Optical emission spectroscopy. *Analytical Chemistry,* **46**(13):1110A-1120a.

Ferla, P., and Meli, C. (2006). Evidence of magma mixing in the 'Daly Gap'of alkaline suites: a case study from the enclaves of Pantelleria (Italy). *Journal of Petrology*, **47**(8):1467-1507.

Fontijn, K., Elburg, M., Nikogosian, I., van Bergen, M., and Ernst, G. (2013). Petrology and geochemistry of Late Holocene felsic magmas from Rungwe volcano (Tanzania), with implications for trachytic Rungwe Pumice eruption dynamics. *Lithos*, **177:**34-53.

Fontijn, K., McNamara, K., Zafu Tadesse, A., Pyle, D.M., Dessalegn, F., Hutchison, W., Mather, T.A., and Yirgu, G. (2018). Contrasting styles of post-caldera volcanism along the Main Ethiopian Rift: Implications for contemporary volcanic hazards. *Journal of Volcanology and Geothermal Research*; https://doi.org/10.1016/j.jvolgeores.2018.02.001

Frey, F. A., Green, D. H., and Roy, S. D. (1978). Integrated models of basalt petrogenesis: a study of quartz tholeiites to olivine melilitites from south eastern Australia utilizing geochemical and experimental petrological data. *Journal of petrology,* **19**(3):463-513.

Furman, T., Bryce, J., Rooney, T., Hanan, B., Yirgu, G., and Ayalew, D. (2006). Heads and tails: 30 million years of the Afar plume. *Geological Society, London, Special Publications*, **259**(1):95-119.

Gasparon, M., Innocenti, F., Manetti, P., Peccerillo, A., and Abebe, T. (1993). Genesis of the Pliocene to Recent bimodal mafic-felsic volcanism in the Debre Zeyt area, central Ethiopia: volcanological and geochemical constraints. *Journal of African Earth Sciences (and the Middle East),* **17**(2):145-165.

870 Giordano, F., D'Antonio, M., Civetta, L., Tonarini, S., Orsi, G., Ayalew, D., Yirgu, G.,
871 Dell'Erba, F., Di Vito, M.A., and Isaia, R. (2014). Genesis and evolution of mafic and
872 felsic magmas at Quaternary volcanoes within the Main Ethiopian Rift: Insights from
873 Gedemsa and Fanta'Ale complexes. *Lithos,* **188**:130-144.
874 Gualda, G. A., Ghiorso, M. S., Lemons, R. V., and Carley, T. L. (2012). Rhyolite-MELTS: a
875 modified calibration of MELTS optimized for silica-rich, fluid-bearing magmatic
876 systems. *Journal of Petrology*, **53**(5):875-890.
877 Hay, D. E., and Wendlandt, R. F. (1995). The origin of Kenya rift plateau-type flood
878 phonolites: Results of high-pressure/high-temperature experiments in the systems
879 phonolite-H_2O and phonolite-H_2O-CO_2. *Journal of Geophysical Research: Solid*
880 *Earth*, **100**(B1):401-410.
881 Hayward, N. and Ebinger, C. (1996). Variations in the along-axis segmentation of the Afar
882 Rift system. *Tectonics,* **15**(2):244-257.
883 Hofmann, A.W. (2003). Sampling mantle heterogeneity through oceanic basalts: isotopes
884 and trace elements. In: Carlson, R.W. (Ed.), Treatise on Geochemistry. The Mantle
885 and Core vol. 3. Elsevier, New York, pp. 61–101.
886 Hofmann, A. W., Jochum, K. P., Seufert, M., and White, W. M. (1986). Nb and Pb in oceanic
887 basalts: new constraints on mantle evolution. *Earth and Planetary science*
888 *letters,* **79**(1-2):33-45.
889 http://ethiopianrift.igg.cnr.it/utilities_MER.html retrieved on the date 25-Oct-2016
890 Hutchison, W., Mather, T. A., Pyle, D. M., Boyce, A. J., Gleeson, M. L., Yirgu, G, Blundy,
891 J.D, Ferguson, J.D, Vye-Brown, C., Millar, L.I., Sims, K. W., and Finch, A.A. (2018).
892 The evolution of magma during continental rifting: New constraints from the isotopic
893 and trace element signatures of silicic magmas from Ethiopian volcanoes. *Earth and*
894 *Planetary Science Letters*, **489**:203-218.
895 Hutchison, W., Pyle, D.M., Mather, T.A., Yirgu, G., Biggs, J., Cohen, B.E., Barfod, D.N.,
896 and Lewi, E. (2016). The eruptive history and magmatic evolution of Aluto volcano:
897 new insights into silicic peralkaline volcanism in the Ethiopian rift. *Journal of*
898 *Volcanology and Geothermal Research,* **328**:9-33.
899 Irvine, T., and Baragar, W. (1971). A guide to the chemical classification of the common
900 volcanic rocks. *Canadian journal of earth sciences,* **8**(5):523-548.
901 Jones, W. B. (1979). Mixed benmoreite/trachyte flows from Kenya and their bearing on the
902 Daly Gap. *Geological Magazine,* **116**(6):487-489.

Keir, D., Ebinger, C. J., Stuart, G. W., Daly, E., and Ayele, A. (2006). Strain accommodation by magmatism and faulting as rifting proceeds to breakup: Seismicity of the northern Ethiopian rift. *Journal of Geophysical Research: Solid Earth*, **111**(B5).

Keranen, K., Klemperer, S. L., Gloaguen, R., and Group, E. W. (2004). Three-dimensional seismic imaging of a protoridge axis in the Main Ethiopian rift. *Geology*, **32**(11):949-952.

Keranen, K. M., Klemperer, S. L., Julia, J., Lawrence, J. F., and Nyblade, A. A. (2009). Low lower crustal velocity across Ethiopia: Is the Main Ethiopian Rift a narrow rift in a hot craton? *Geochemistry, Geophysics, Geosystems*, **10**(5).

Kieffer, B., Arndt, N., Lapierre, H., Bastien, F., Bosch, D., Pecher, A., Yirgu, G., Ayalew, D., Weis, D., Jerram, D. A., Keller, F., and Meugniot, C. (2004). Flood and shield basalts from Ethiopia: Magmas from the African superswell. *Journal of Petrology*, **45**(4):793-834.

Kushiro, I. (1996). Partial melting of a fertile mantle peridotite at high pressures: an experimental study using aggregates of diamond. *Earth processes: Reading the isotopic code*, 109-122.

Le Bas, M. J., Le Maitre, R., Streckeisen, A., and Zanettin, B. (1986). A chemical classification of volcanic rocks based on the total alkali-silica diagram. *Journal of Petrology*, **27**(3):745-750.

Lowenstern, J. B., Charlier, B. L. A., Clynne, M. A., and Wooden, J. L. (2006). Extreme U–Th disequilibrium in rift-related basalts, rhyolites and granophyric granite and the timescale of rhyolite generation, intrusion and crystallization at Alid Volcanic Center, Eritrea. *Journal of Petrology*, **47**(11):2105-2122.

Macdonald, R. (1974). Nomenclature and petrochemistry of the peralkaline oversaturated extrusive rocks. *Bulletin Volcanologique*, **38**(2):498-516.

Macdonald, R., Bagiński, B., Ronga, F., Dzierżanowski, P., Lustrino, M., Marzoli, A., and Melluso, L. (2012). Evidence for extreme fractionation of peralkaline silicic magmas, the Boseti volcanic complex, Main Ethiopian Rift. *Mineralogy and Petrology*, **104**(3-4):163-175.

Macdonald, R., Belkin, H. E., Fitton, J. G., Rogers, N. W., Nejbert, K., Tindle, A. G., and Marshall, A. S. (2008). The roles of fractional crystallization, magma mixing, crystal mush remobilization and volatile–melt interactions in the genesis of a young basalt–peralkaline rhyolite suite, the Greater Olkaria Volcanic Complex, Kenya Rift Valley. *Journal of Petrology*, **49**(8):1515-1547.

Macgregor, D. (2015). History of the development of the East African Rift System: A series of interpreted maps through time. *Journal of African Earth Sciences*, **101:**232-252.

Mackenzie, G., Thybo, H., and Maguire, P. (2005). Crustal velocity structure across the Main Ethiopian Rift: results from two-dimensional wide-angle seismic modelling. *Geophysical Journal International*, **162**(3):994-1006.

Mahatsente, R., Jentzsch, G., and Jahr, T. (1999). Crustal structure of the Main Ethiopian Rift from gravity data: 3-dimensional modeling. *Tectonophysics*, **313**(4):363-382.

Maguire, P. K. H., Keller, G. R., Klemperer, S. L., Mackenzie, G. D., Keranen, K., Harder, S., O'Reilly, B., Thybo, H., Asfaw, L., Khan, M.A., and Amha, M. (2006). Crustal structure of the northern Main Ethiopian Rift from the EAGLE controlled-source survey; a snapshot of incipient lithospheric break-up. *Geological Society, London, Special Publications*, **259**(1):269-292.

Marsh, B. D. (1981). On the crystallinity, probability of occurrence, and rheology of lava and magma. *Contributions to Mineralogy and Petrology*, **78**(1):85-98.

Mazzarini, F., Le Corvec, N., Isola, I., and Favalli, M. (2016). Volcanic field elongation, vent distribution, and tectonic evolution of a continental rift: The Main Ethiopian Rift example. *Geosphere*, **12**(3):706-720

McDonough, W. F., and Sun, S.S. (1995). The composition of the Earth. *Chemical Geology*, **120**(3):223-253.

Mohr, P. (1971). Ethiopian Rift and plateaus: some volcanic petrochemical differences. *Journal of Geophysical Research*, **76**(8):1967-1984.

Mohr, P. (1983a). The Morton-Black hypothesis for the thinning of continental crust revisited in western Afar. *Tectonophysics*, **94**(1):509-528.

Mohr, P. (1983b). Volcanotectonic aspects of Ethiopian rift evolution. *Bulletin Centre Recherches Elf Aquitaine Exploration Production*, **7:**175-189.

Mohr, P., and Zanettin, B. (1988). The Ethiopian flood basalt province. **In**: *Continental flood basalts*, pp. 63-110: Springer, Netherlands.

Montaser, A. (1998). *Inductively coupled plasma mass spectrometry*. John Wiley and Sons.

Morley, C. (1999). Tectonic evolution of the East African Rift System and the modifying influence of magmatism. *Acta vulcanologica*, **11:**1-20.

Morton, W. (1979). Riftward younging of volcanic units in the Addis Ababa region, Ethiopian rift valley. *Nature*, **280:**284-288.

Neumann, H., Mead, J., and Vitaliano, C. J. (1954). Trace element variation during fractional crystallization as calculated from the distribution law. *Geochimica et Cosmochimica Acta*, **6**(2-3):90-99.

Peccerillo, A., Barberio, M., Yirgu, G., Ayalew, D., Barbieri, M., and Wu, T. (2003). Relationships between mafic and peralkaline silicic magmatism in continental rift settings: a petrological, geochemical and isotopic study of the Gedemsa volcano, central Ethiopian rift. *Journal of Petrology*, **44**(11).

Peccerillo, A., Donati, C., Santo, A., Orlando, A., Yirgu, G., and Ayalew, D. (2007). Petrogenesis of silicic peralkaline rocks in the Ethiopian rift: geochemical evidence and volcanological implications. *Journal of African Earth Sciences*, **48**(2):161-173.

Pik, R., Deniel, C., Coulon, C., Yirgu, G., and Marty, B. (1999). Isotopic and trace element signatures of Ethiopian flood basalts: evidence for plume–lithosphere interactions. *Geochimica et Cosmochimica Acta*, **63**(15):2263-2279.

Rampey, M.L., Oppenheimer, C., Pyle, D.M., and Yirgu, G., (2010). Caldera-forming eruptions of the Quaternary Kone Volcanic Complex, Ethiopia. *Journal of African Earth Sciences*, **58**(1):51-66.

Rapprich, V., Žáček, V., Verner, K., Erban, V., Goslar, T., Bekele, Y., Legesa, F., Hroch, T., and Hejtmánková, P. (2016). Wendo Koshe Pumice: the latest Holocene silicic explosive eruption product of the Corbetti Volcanic System (Southern Ethiopia). *Journal of Volcanology and Geothermal Research*, **310**:159-171.

Ring, U. (2014). The East African Rift System. *Austrian J Earth Sci*, **107**(1):132-146.

Ronga, F., Lustrino, M., Marzoli, A., and Melluso, L. (2010). Petrogenesis of a basalt-comendite-pantellerite rock suite: the Boseti Volcanic Complex (Main Ethiopian Rift). *Mineralogy and Petrology*, **98**(1-4):227-243.

Rooney, T. (2010). Geochemical evidence of lithospheric thinning in the southern Main Ethiopian Rift. *Lithos*, **117**(1):33-48.

Rooney, T. (2017). The Cenozoic magmatism of East-Africa: Part I — Flood basalts and pulsed magmatism. *Lithos*, **286–287**:264-301.

Rooney, T. O., Bastow, I. D., and Keir, D. (2011). Insights into extensional processes during magma assisted rifting: Evidence from aligned scoria cones. *Journal of Volcanology and Geothermal Research*, **201**(1-4):83-96.

Rooney, T., Furman, T., Bastow, I., Ayalew, D., and Yirgu, G. (2007). Lithospheric modification during crustal extension in the Main Ethiopian Rift. *Journal of Geophysical Research: Solid Earth*, **112**(B10).

1003 Rooney, T. O., Nelson, W. R., Dosso, L., Furman, T., and Hanan, B. (2014). The role of
1004 continental lithosphere metasomes in the production of HIMU-like magmatism on the
1005 northeast African and Arabian plates. *Geology*, **42**(5):419-422.
1006 Rudnick, R. L., and Gao, S. (2003). Composition of the continental crust. In Treatise on
1007 geochemistry (eds. H.D. Holland and K.K. Turekian), Elsevier-Pergamon,
1008 Oxford, **3**:659.
1009 Saria, E., Calais, E., Stamps, D.S., Delvaux, D., and Hartnady, C.J.H. (2014). Present-day
1010 kinematics of the East African Rift. *Journal of Geophysical Research: Solid Earth,*
1011 **119**(4):3584-3600.
1012 Siegburg, M., Gernon, T. M., Bull, J. M., Keir, D., Barfod, D. N., Taylor, R. N., Abebe, B.,
1013 and Ayele, A. (2018). Geological evolution of the Boset-Bericha Volcanic Complex,
1014 Main Ethiopian Rift: 40Ar/39Ar evidence for episodic Pleistocene to Holocene
1015 volcanism. *Journal of Volcanology and Geothermal Research*, **351**:115-133.
1016 Stormer Jr, J. C., and Nicholls, J. (1978). XLFRAC: a program for the interactive testing of
1017 magmatic differentiation models. *Computers & Geosciences*, **4**(2):143-159.
1018 Taylor SR., and McLennan SM. (1985). The continental crust: its composition and evolution.
1019 Blackwell Scientific Publication, Carlton, 312 p.
1020 Teklay, M., Kröner, A., Mezger, K., and Oberhänsli, R. (1998). Geochemistry, Pb-Pb single
1021 zircon ages and Nd-Sr isotope composition of Precambrian rocks from southern and
1022 eastern Ethiopia: implications for crustal evolution in East Africa. *Journal of African*
1023 *Earth Sciences,* **26**(2):207-227.
1024 Thy, P., Beard, J. S. and Lofgren, G. E. (1990). Experimental constraints on the origin of
1025 Icelandic rhyolites. *The Journal of Geology*, **98**(3):417-421.
1026 Trua, T., Deniel, C., and Mazzuoli, R. (1999). Crustal control in the genesis of Plio-
1027 Quaternary bimodal magmatism of the Main Ethiopian Rift (MER): geochemical and
1028 isotopic (Sr, Nd, Pb) evidence. *Chemical Geology,* **155**(3):201-231.
1029 Weissel, J. K., and Karner, G. D. (1989). Flexural uplift of rift flanks due to mechanical
1030 unloading of the lithosphere during extension. *J. geophys. Res*, **94**(B10):13919-13950.
1031 Woldegabriel, G., Aronson, J. L., and Walter, R. C. (1990). Geology, geochronology, and rift
1032 basin development in the central sector of the Main Ethiopia Rift. *Geological Society*
1033 *of America Bulletin,* **102**(4):439-458.
1034 Wolfenden, E., Ebinger, C., Yirgu, G., Deino, A., and Ayalew, D. (2004) Evolution of the
1035 northern Main Ethiopian Rift: Birth of a Triple Junction. *Earth and Planetary Science*
1036 *Letters,* **224**:213-228.

Figure Captions

Figure 1: Digital elevation model showing the north-central segment of the MER and its bounding plateau (Eastern and Western Plateau). The fault lines are from http://ethiopianrift.igg.cnr.it/utilities_MER.html.

Figure 2: (A) Sketch geological map of the study area (modified after Damte et al., 1992). (B) Geological cross-section along A-A' traverse line. The scale for the vertical axis in the geological cross-section is labeled in meters. The vertical scale is two times exaggerated. (C) Composite stratigraphy of BVC.

Figure 3: Pumice flow exposures at base of the Dabe section (A) and the southern tip of Boku ridge (B). Note that in figure "A" the lithic fragments are rhyolite and obsidian lava (indicated by an arrow). On "B" the outcrop shows intercalation of ash flow with pumice flow layers underlain by basaltic lava flows (Qbl). Pumice fall is exposed on the Dabe section interbeded between ash flow deposits. C) Dabe section showing interbedding of pumice fall layer between ash flows.

Figure 4: Litho-stratigraphic correlation between BVC and Nazret-Dera area. The Nazret-Dera area volcanic stratigraphy is after Boccaletti et al. (1999).

Figure 5: TAS diagram for BVC after Le Bas et al. (1986). The dashed line separates the alkaline from subalkaline series (Irvine and Baragar, 1971). The major element data are normalized under volatile-free base out of 100%. The grey field shows previously published whole-rock chemical data for other MER volcanoes (Rapprich et al., 2016; Giordano et al., 2014; Boccaletti et al., 1995; Chernet and Hart, 1999; Gasparon et al., 1993; Peccerillo et al., 2003; 2007; Ronga et al., 2010; Rooney 2010; Rooney et al., 2011; Rooney et al., 2014; Rooney et al., 2007; Hutchison et al., 2016). The grey field encloses predominant mafic and felsic rocks with rare rocks of intermediate composition, specifically at Boset and Aluto (Ronga et al., 2010; Hutchison et al., 2016; 2018; Seigburg et al., 2018).

Figure 6: A) Classification of silicic volcanic products from BVC after Le Bas et al. (1986). B) Classification diagram of peralkaline silicic rocks (after Macdonald, 1974).

Figure 7: Selected major element Harker diagrams of BVC whole-rock compositions.

Figure 8: Selected trace element variation diagrams against SiO_2.

Figure 9: Selected trace element plot against Zr.

Figure 10: (A) REE variation diagram of representative samples from mafic and silicic rocks. The concentrations are normalized to chondrite values (Boynton, 1984). (B) Multi-element spider diagram of representative mafic and silicic rocks of BVC. The concentrations are normalized to the primordial mantle value determined by McDonough and Sun (1995).

Figure 11: La/Nb (A) and Th/Ta against SiO_2 (B) diagrams of rock samples collected from Boku volcano and adjacent volcanoes (Gedemsa and Fenta'Ale after Giordano et al., 2014). (C) and (D) plots show the trace element ratios (Rb/Nb and Rb/Zr) of BVC samples compared with Ethiopian flood basalt (EFB) and Precambrian rocks (M-BR: metamorphic basement rock and C-BR: crystallized or plutonic basement rock). The data in diagram "C" and "D" is adopted from Alene et al. (2000), Teklay et al. (1998), Asrat and Barbey (2003) and Kieffer et al. (2004).

Figure.12: (A**)** Rb vs. Sr diagram to highlight the degree of variations in incompatible versus compatible element concentrations. (B) Trace element modeling. The partition coefficients used in the model for Sr and Rb are adopted from Ewart and Griffin (1994). Fractional crystallization model by applying the equation of Neuman et al. (1954) to see trace element at 80% fractionation displayed on REE (C) and spidergram (D) plot.

Figure 13. Different graphs illustrating petrogenetic modelling of peralakaline silicic rocks. A) SiO_2 against temperature graph for selected different pressure conditions. B) The classification plot after LeBas et al. (1986) of the remaining melt at different pressure conditions. C) Mass proportion of different mineral phases crystallizing in function of temprature at 0.6 kbar. D) Schematic diagram illustrating progressive evolution of mafic melts sourced from the upper mantle. Depth extent of the partial melting and depth of melt ponding at shallow crust levels is inferred from geophysical and geochemical studies (e.g. Ayalew and Gibson, 2009; Dugda et al., 2005; Rooney et al., 2011; Keranen et al., 2009; Keranen et al., 2004).

Tables

Table 1: Geochemical data of BVC samples; the major element (including LOI) and trace element concentrations are expressed in wt% and ppm respectively. The major element data is normalized to 100% at volatile-free base. AI** is Agpaitic index calculated as molecular ($\frac{Al_2O_3}{Na_2O+K_2O}$) and L.D* is the ICP-MS limit of detection for different trace elements. The CIPW norm values for the selected minerals are the percentage calculated from the chemical analysis based on the rule of norm calculation after Cross et al. (1903).

Sample	**NB-01**	**NB-07**	**NB-02**	**NB-03**	**NB-08**	**NB-05**	**NB-06**	**NB-04**
Lithology	**Basalt**	**Basalt**	**Basalt**	**Scoria**	**Scoria**	**Basalt**	**Basalt**	**Basalt**
ICP-OES (wt%)								
SiO_2	45.43	46.62	47.3	47.58	47.93	48.13	49.29	49.37
TiO_2	2.19	2.20	2.29	2.01	1.69	1.97	1.93	1.90
Al_2O_3	16.81	14.89	15.84	15.44	14.68	15.84	17.26	15.79
FeO_t	11.46	11.04	10.98	10.61	9.93	10.63	11.26	10.53
MnO	0.19	0.18	0.19	0.18	0.17	0.18	0.18	0.18
MgO	8.81	9.02	7.81	8.81	9.77	7.9	5.79	7.08
CaO	10.52	11.17	10.73	10.52	11.48	10.22	9.84	9.65
Na_2O	2.52	2.65	2.66	2.67	2.3	2.75	3.11	3.00
K_2O	0.46	0.59	0.67	0.67	0.58	0.86	0.92	1.00
P_2O_5	0.33	0.42	0.35	0.36	0.38	0.35	0.29	0.34
Total	98.72	98.78	98.82	98.85	98.91	98.83	98.87	98.84
LOI	1.76	0.16	1.79	0.44	1.52	0.64	1.37	0.26
Norm (wt %)								
Quartz								
Albite	18.13	18.76	22.29	22.4	19.46	23.27	26.32	25.38
Diopside	13.99	21.21	17.98	17.92	21.7	16.69	13.87	15.88
Hypersthene					2.74	1.37	4.47	4.92
Olivine	24.05	21.21	20.03	21.66	19.48	19.54	14.05	15.72
Nepheline	1.73	1.98	0.12	0.1				
Acmite								
AI**								
ICP-MS (ppm)								
Be	1.121	0.779	1.051	0.985	0.886	0.963	1.082	1.126
Sc	34.86	34.48	32.87	32.89	33.57	32.95	30.33	29.51
V	216	284.1	283.9	263.2	233.6	263.1	266.8	238.6

Cr	368.6	581.3	391.8	392.2	573.8	392.6	157.7	263.2
Co	49.62	49.35	46.66	48.33	48.12	47.28	37.91	43.08
Ni	87.92	143.4	114.6	75.11	153.7	72.93	30.69	53.49
Cu	51.92	72.91	76.48	37.62	89.72	36.28	25.52	37.22
Zn	109.8	97.09	116.2	113	85.96	101.9	97.41	107.1
Rb	3.073	6.691	7.675	10.75	10.62	12.21	13.88	15.82
Sr	433.8	447	441.7	455.9	346.5	441.5	454.7	476.3
Y	23.21	21.76	19.59	20.86	16.98	21.29	21.78	23.15
Zr	133.6	107.6	115.3	124.1	93.79	124.7	127.1	137.7
Nb	23.72	18.45	17.79	21.97	14.41	21.95	20.64	20.11
Sn	1.667	1.351	1.732	1.394	1.254	1.407	1.516	1.815
Cs	< L.D.*	< L.D.	0.023	0.097	0.018	< L.D.	< L.D.	0.129
Ba	254.1	267.1	257.8	250.6	189.2	323.4	268.9	458.6
La	21.27	17.52	15.69	19.11	12.2	19.78	18.35	21.17
Ce	43.67	36.59	34.42	41.31	27.42	41.63	38.98	42.95
Pr	5.746	5.008	4.536	5.278	3.665	5.475	5.142	5.668
Nd	23.92	21.35	19.36	22.18	15.88	22.66	21.24	23.36
Sm	5.329	4.866	4.443	4.877	3.708	4.972	4.703	5.177
Eu	1.855	1.767	1.559	1.703	1.314	1.716	1.653	1.84
Gd	4.901	4.678	4.229	4.5	3.537	4.575	4.382	4.808
Tb	0.746	0.693	0.635	0.678	0.537	0.684	0.677	0.717
Dy	4.49	4.142	3.802	4.071	3.285	4.113	4.087	4.331
Ho	0.908	0.833	0.771	0.822	0.664	0.827	0.832	0.876
Er	2.327	2.084	1.951	2.065	1.67	2.111	2.149	2.238
Tm	0.31	0.281	0.265	0.285	0.232	0.286	0.303	0.308
Yb	2.072	1.799	1.735	1.872	1.507	1.89	1.991	2.011
Lu	0.319	0.271	0.259	0.285	0.233	0.284	0.302	0.306
Hf	3.506	2.822	3.02	3.315	2.5	3.312	3.436	3.642
Ta	1.809	1.42	1.351	1.666	1.104	1.667	1.601	1.539
Pb	2.53	2.1306	3.3679	2.5829	2.2527	2.7221	2.5731	4.2856
Th	2.231	1.572	1.651	2.134	1.355	2.187	2.391	2.576
U	0.211	0.291	0.328	0.514	0.383	0.377	0.4	0.674

1114

1115

1116

1117

1118

1119

1120

1121 Table 1 continued

Sample	NB-11	NB-12	NB-10	NB-13	NB-16	NB-15	NB-14	NB-09
Lithology	**Rhyolite**	**Rhyolite**	**Rhyolite**	**Rhyolite**	**Rhyolite**	**Rhyolite**	**Rhyolite**	**Rhyolite**
ICP-OES (wt %)								
SiO_2	70.23	70.9	71.12	71.65	73.16	73.3	74.7	75.45
TiO_2	0.5	0.44	0.44	0.42	0.39	0.19	0.26	0.19
Al_2O_3	11.53	11.02	11.61	10.59	9.97	13.68	9.47	10.88
FeO_t	5.62	5.76	6.46	5.86	6.34	2.29	5.17	4.09
MnO	0.31	0.33	0.25	0.38	0.3	0.02	0.17	0.10
MgO	0.25	0.13	0.10	0.19	0.07	0.07	0.07	0.05
CaO	0.34	0.34	0.15	0.44	0.33	0.18	0.29	0.12
Na_2O	5.83	5.85	4.22	5.19	4.22	4.91	4.88	3.8
K_2O	4.75	4.59	4.92	4.64	4.52	5.1	4.43	4.87
P_2O_5	< L.D.	< L.D.	< L.D.	< L.D.	< L.D.	< L.D.	< L.D.	< L.D.
Total	99.36	99.36	99.27	99.36	99.30	99.74	99.44	99.55
LOI	0.65	0.43	1.53	0.81	1.52	0.88	0.73	0.85
Norm (wt %)								
Quartz	22.19	24.45	24.03	26.74	31.02	23.04	34.49	32.97
Albite	32.86	31.13	32.33	28.64	26.12	41.55	24.05	28.85
Diopside	1.56	1.55	0.7	2	1.51	0.66	1.29	0.54
Hypersthene	9.87	9.96	11.47	10.18	10.93	3.74	8.87	7.22
Olivine								
Nepheline								
Acmite	14.51	16.18	2.98	13.46	8.46		15.19	2.91
AI	1.09	1.06	1.27	1.08	1.14	1.37	1.02	1.26
ICP-MS (ppm)								
Be	4.873	5.02	5.052	4.647	5.07	3.843	8.043	6.035
Sc	8.19	6.08	5.47	5.13	< L.D.	3.61	< L.D.	< L.D.
V	2.861	1.434	1.863	1.608	0.955	3.992	2.037	4.532
Cr	26.87	17.13	19.83	63.05	15.31	31.35	54.76	24.92
Co	0.332	0.209	0.274	0.365	0.152	0.269	0.365	0.386
Ni	< L.D.	< L.D.	< L.D.	< L.D.	< L.D.	< L.D.	< L.D.	< L.D.
Cu	< L.D.	< L.D.	< L.D.	< L.D.	< L.D.	< L.D.	13.4	< L.D.
Zn	197.9	211.2	192.9	215.7	245.8	87.97	261	176.4
Rb	109.4	107.9	118	118.1	131.1	129	199.1	197.5
Sr	7.062	5.131	8.924	13.84	5.727	12.16	7.829	8.33
Y	55.61	86.34	97.45	64.75	60.53	45.96	89.1	97.57
Zr	662.3	660.4	729.7	684.7	791.4	557.4	958.5	980
Nb	86.59	86.68	94.61	87.79	108.4	57.02	145.6	108.4
Sn	5.925	6.109	6.956	6.209	7.852	5.968	10.23	10.42

Cs	0.659	0.88	0.175	0.439	0.319	0.615	1.442	0.402
Ba	374.1	267.9	228.6	348	280.5	345.5	26.74	46.5
La	75.43	90.7	117.6	76.06	68.48	66.12	90.46	75.94
Ce	160.6	158.4	202.1	199.8	215.1	95.39	219	234.1
Pr	20.12	21.03	29.32	19.73	18.98	16.22	19.15	20.8
Nd	74.51	78.73	109.1	74.05	69.12	57.06	68.38	76.43
Sm	14.82	15.88	20.96	14.83	14.01	10.55	13.78	18.23
Eu	3.383	3.626	4.475	3.262	2.943	0.899	1.494	1.438
Gd	11.83	14.47	17.03	12.59	11.4	8.066	12.96	16.94
Tb	1.925	2.363	2.832	2.057	2.012	1.342	2.244	2.983
Dy	11.82	14.9	17.98	12.89	13.18	8.343	15.11	19.34
Ho	2.338	3.13	3.76	2.682	2.786	1.75	3.292	4.064
Er	6.19	8.348	10.03	7.218	7.881	4.901	9.104	10.88
Tm	0.937	1.233	1.461	1.058	1.217	0.746	1.369	1.634
Yb	6.539	8.49	9.846	7.132	8.716	5.249	9.585	11.22
Lu	1.047	1.338	1.519	1.124	1.347	0.83	1.522	1.684
Hf	15.97	15.8	17.39	16.56	21.41	14.12	26.69	27.19
Ta	6.481	6.426	6.952	6.663	8.067	4.473	10.49	8.431
Pb	15.2845	13.3516	17.598	15.947	21.7491	13.2812	27.5783	28.9164
Th	12.92	12.62	13.92	13.82	16.98	14.09	24.33	21.85
U	1.618	1.563	0.971	2.525	0.868	2.576	1.126	1.691

1122
1123
1124 Table 1 continued

Sample	**NB-23**	**NB-24**	**NB-20**	**NB-21**	**NB-19**	**NB-22**	**NB-18**	**NB-17**
Lithology	**Ignimbrite**	**Ignimbrite**	**Obsidian**	**Obsidian**	**Obsidian**	**Obsidian**	**Rhyolite**	**Rhyolite**
ICP-OES (wt%)								
SiO_2	68.43	70.27	70.51	70.65	70.86	71.9	73.13	75.4
TiO_2	0.79	0.5	0.50	0.48	0.48	0.42	0.19	0.20
Al_2O_3	12.87	10.7	10.87	11.15	11.19	10.45	13.66	10.96
FeO_t	5.18	5.91	5.73	5.45	5.48	5.86	2.32	4.08
MnO	0.23	0.34	0.31	0.30	0.30	0.32	0.07	0.04
MgO	0.79	0.42	0.20	0.20	0.20	0.09	0.10	0.06
CaO	1.08	0.84	0.30	0.30	0.30	0.31	0.21	0.22
Na_2O	5.71	5.78	6.40	6.37	6.38	5.25	4.94	3.53
K_2O	4.36	4.59	4.53	4.53	4.53	4.76	5.11	5.04
P_2O_5	< L.D.	< L.D.	< L.D.	< L.D.	< L.D.	< L.D.	< L.D.	< L.D.
Total	99.44	99.35	99.35	99.43	99.72	99.36	99.73	99.57
LOI	0.79	1.60	-0.05	0.08	0.00	2.51	0.44	1.74

Norm (wt%)								
Quartz	15.86	23.77	24.03	23.6	23.66	27.61	22.56	32.79
Albite	41.92	29.48	30.69	30.69	32.34	27.25	41.8	28.31
Diopside	4.75	3.73	1.38	1.38	1.39	1.42	0.98	0.98
Hypersthene	8.14	9.74	10.04	9.54	9.59	10.13	3.81	6.86
Olivine								
Nepheline								
Acmite	5.63	17.11	18.43	17.53	17.62	15.43		1.37
AI	1.28	1.03	1	1.02	1.03	1.04	1.36	1.29
ICP-MS (ppm)								
Be	4.042	4.636	4.429	4.54	4.499	5.091	4.175	5.267
Sc	13.25	7.35	7.94	7.93	8.06	4.91	3.8	< L.D.
V	36.27	2.962	1.709	1.616	1.67	0.66	5.152	6.634
Cr	59.66	31.66	22.78	30.66	39.83	19.61	50.92	24.96
Co	4.624	0.313	0.225	0.127	0.225	0.073	0.405	0.119
Ni	< L.D.	< L.D.	< L.D.	< L.D.	< L.D.	< L.D.	< L.D.	< L.D.
Cu	6.245	< L.D.	< L.D.	9.905	< L.D.	< L.D.	< L.D.	< L.D.
Zn	180.3	212.5	208.9	199.4	193.2	222.3	83.54	189.7
Rb	90.87	106.1	106.5	108.2	103.7	122	127.3	195.3
Sr	56.11	13.05	2.189	2.411	2.306	3.723	11.73	13.53
Y	71.28	77.81	76.57	76.7	73.96	84.69	52.12	96.69
Zr	565	652.2	646.8	644.6	618.2	706.1	544.5	946.2
Nb	75.24	88.16	87.26	86.32	83.17	91.63	55.74	106
Sn	5.007	5.992	6.011	5.991	5.722	6.465	5.018	8.543
Cs	0.95	0.931	1.573	1.559	1.476	1.874	0.751	0.269
Ba	574.6	370.3	333.2	405.9	390.7	293.8	346.4	19.41
La	76.53	101.7	78.91	81.09	75.38	87.64	64.1	106
Ce	144.8	166.5	172.5	175.1	167.9	189.5	133.1	210.5
Pr	18.56	22.66	19.92	20.26	19.4	21.88	15.08	25.72
Nd	69.72	84.3	73.85	76	72.77	83.06	53.64	93.18
Sm	14.32	16.74	15.36	15.34	14.81	17.09	10.24	20.01
Eu	3.116	3.797	3.569	3.562	3.438	3.777	0.853	1.322
Gd	12.35	14.03	13.16	13.33	12.78	14.91	8.541	17.42
Tb	2.068	2.326	2.21	2.214	2.13	2.461	1.4	2.815
Dy	12.86	14.32	13.91	13.92	13.38	15.37	8.83	17.37
Ho	2.737	2.979	2.957	2.932	2.818	3.267	1.877	3.681
Er	7.359	8.081	7.93	7.869	7.621	8.667	5.181	9.896
Tm	1.081	1.188	1.17	1.163	1.101	1.275	0.773	1.451
Yb	7.314	8.12	7.913	7.857	7.441	8.612	5.39	9.737
Lu	1.111	1.232	1.215	1.192	1.144	1.317	0.841	1.471

Hf	13.66	15.96	15.63	15.66	14.98	17.26	13.59	26.18
Ta	5.464	6.487	6.398	6.354	6.076	6.787	4.361	8.117
Pb	12.9708	14.2818	15.3291	15.5061	14.7386	17.1482	13.4227	14.5133
Th	10.07	13.02	12.78	12.68	12.23	14.21	13.67	21.18
U	2.234	2.235	2.982	2.936	2.859	3.218	2.367	2.443

1125

1126 Table 1 continued

Sample	**NB-29**	**NB-27**	**NB-26**	**NB-25**	**NB-30**	**NB-28**
Lithology	**Pumice**	**Pumice**	**Pumice**	**Pumice**	**Pumice**	**Pumice**
ICP-OES (wt%)						
SiO_2	68.93	70.33	71.59	72.7	73.01	73.09
TiO_2	0.28	0.45	0.47	0.46	0.44	0.38
Al_2O_3	7.75	16.07	11.7	11.46	10.86	10.43
FeO_t	8.04	3.28	6.52	6.41	6.06	6.04
MnO	0.35	0.07	0.33	0.34	0.33	0.28
MgO	0.22	0.88	0.43	0.21	0.12	0.1
CaO	3.98	1.04	1.14	0.67	0.4	0.5
Na_2O	5.04	1.74	1.63	2	1.87	1.75
K_2O	4.52	5.78	5.46	5.04	6.25	6.77
P_2O_5	< L.D.	< L.D.	< L.D.	< L.D.	< L.D.	< L.D.
Total	99.11	99.64	99.27	99.29	99.34	99.34
LOI	7.94	9.50	9.08	9.04	7.40	7.03
Norm (wt%)						
Quartz	26.84	32.01	32.67	34.65	32.1	31.12
Albite	14.7	14.72	13.79	16.92	15.82	14.81
Diopside	17.62					1.74
Hypersthene	6.17	7.59	12.89	12.16	11.3	10.31
Olivine						
Nepheline						
Acmite	24.62					
AI	0.81	2.14	1.65	1.63	1.34	1.22
ICP-MS (ppm)						
Be	7.068	4.068	5.187	4.798	4.866	5.373
Sc	< L.D.	5.22	5.55	5.12	4.77	3.01
V	2.439	14.69	1.755	0.707	1.356	1.311
Cr	16.75	13.83	< L.D.	< L.D.	35.46	26.04
Co	0.409	2.303	0.317	0.04	0.248	0.166
Ni	< L.D.	< L.D.	< L.D.	< L.D.	< L.D.	< L.D.
Cu	< L.D.	< L.D.	< L.D.	< L.D.	< L.D.	< L.D.
Zn	334.6	79.04	222.9		217.7	235

Rb	124.6	123.9	198.6	221.4	158.3	178.5
Sr	92.67	117.9	30.25	256	7.489	22.04
Y	136.3	30.72	81.64	52.83	87.5	98.87
Zr	882.5	427.4	722.1	82.59	702.3	713.4
Nb	160.5	41.86	93.56	718.5	89.42	98.76
Sn	9.441	5.412	6.643	93.29	6.449	7.416
Cs	1.189	1.01	2.2	6.577	1.778	1.735
Ba	510.8	447	308.2	2.027	284.9	372
La	131.2	50.43	90.03	282.9	90.11	120.5
Ce	245.4	89.1	194.6	87.62	185.3	222.5
Pr	28.2	10.57	21.91	188.8	21.6	26.53
Nd	108.2	36.8	83.9	21.57	82.06	102
Sm	22.87	6.689	17.41	81.69	16.63	20.87
Eu	5.663	0.859	3.855	16.85	3.729	4.373
Gd	21.26	5.48	15.12	3.738	14.69	18.41
Tb	3.553	0.867	2.482	14.65	2.402	2.957
Dy	22.84	5.409	15.49	2.427	15.09	18.36
Ho	4.926	1.139	3.228	15.17	3.212	3.825
Er	13.16	3.145	8.617	3.194	8.583	10.06
Tm	1.948	0.499	1.275	8.509	1.275	1.459
Yb	13.15	3.502	8.781	1.244	8.548	9.861
Lu	1.959	0.54	1.326	8.521	1.281	1.465
Hf	24.23	11.3	17.42	1.284	16.92	20.21
Ta	11.09	3.726	6.937	17.46	6.669	7.435
Pb	17.337	13.7325	17.6564	6.874	17.0445	19.8169
Th	16.69	14.02	14.68	17.2367	13.96	16.14
U	4.163	2.298	2.933	14.52	3.194	3.314
				3.07		

Table 2: Rb/Nb and Rb/Zr values of BVC samples compared to Ethiopian Precambrian rock and flood basalt data. Northern Ethiopia Precambrian rock data after Alene et al. (2000), Southern and Eastern Precambrian metamorphic rock after Teklay et al. (1998) and Konso pluton data from Asrat and Barbey (2003). The flood basalt data is taken from Kieffer et al. (2004).

	BVC		**Flood Basalt**	**Northern Ethiopia**			**Southern and Eastern Ethiopia**	
	Basaltic rock	Silicic rock		Basic/Intermediate	Acidic	Pluton	Metamorphic rock	Konso Pluton
Rb/Nb	0	0.13-1.37	0.13-2.16	1-6.33	0-5.56	0.6-12.6	0.2-10.07	1.12-5.81
Rb/Zr	0	0.023-0.21	0.0072-0.32	0.048-0.5	0-0.37	0.27-1.8	0.015-0.59	0.085-0.65

Fig. 1

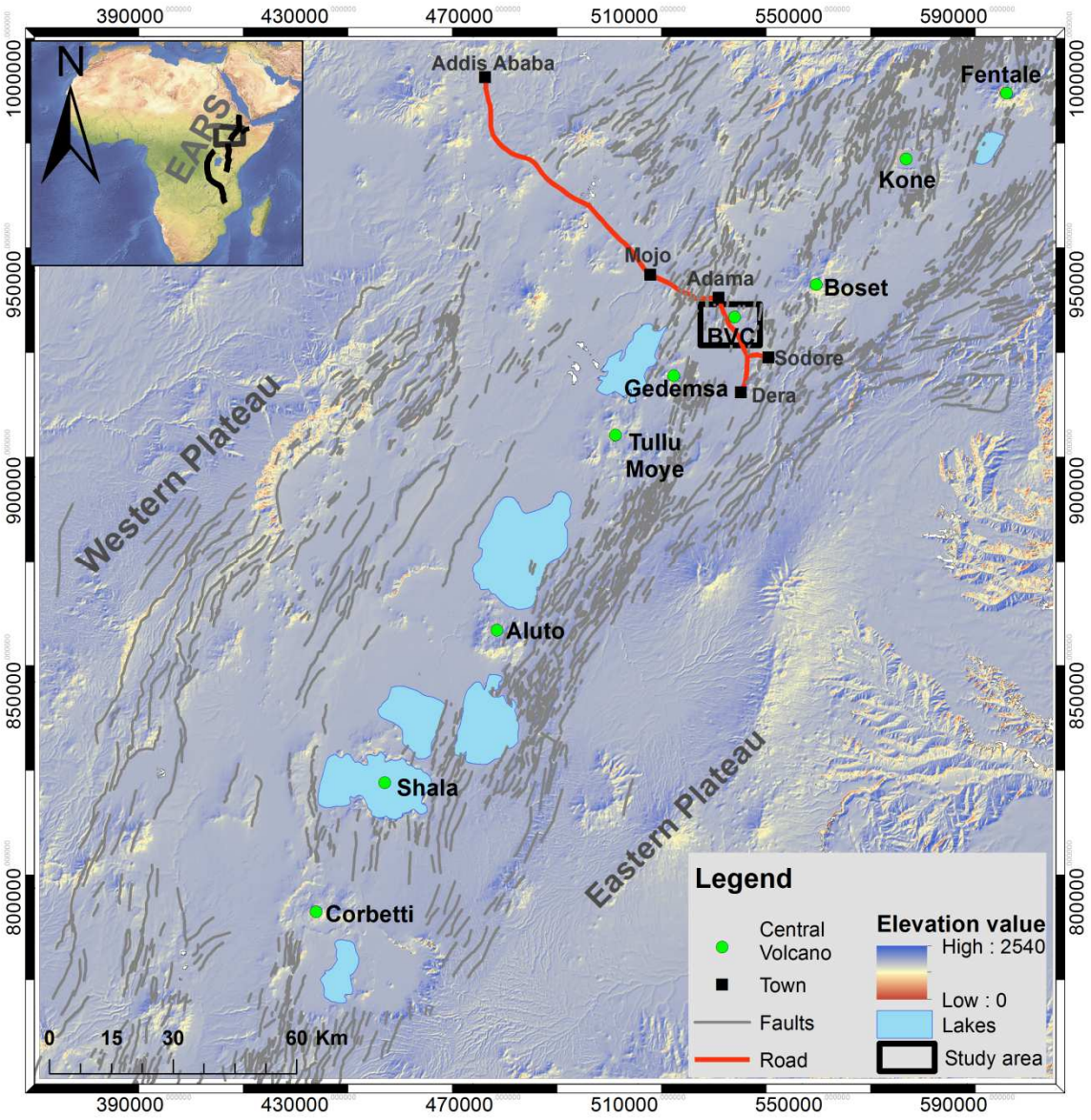
390000
430000
470000
510000
550000
590000
1000000
950000
900000
850000
800000
N
EARS
Addis Ababa
Fentale
Kone
Mojo
Adama
Boset
BVC
Sodore
Gedemsa
Dera
Tullu
Moye
Western Plateau
Aluto
Shala
Eastern Plateau
Corbetti
Legend
Central Volcano
Town
Faults
Road
Elevation value
High : 2540
Low : 0
Lakes
Study area
0
15
30
60 Km

Fig. 2
A)

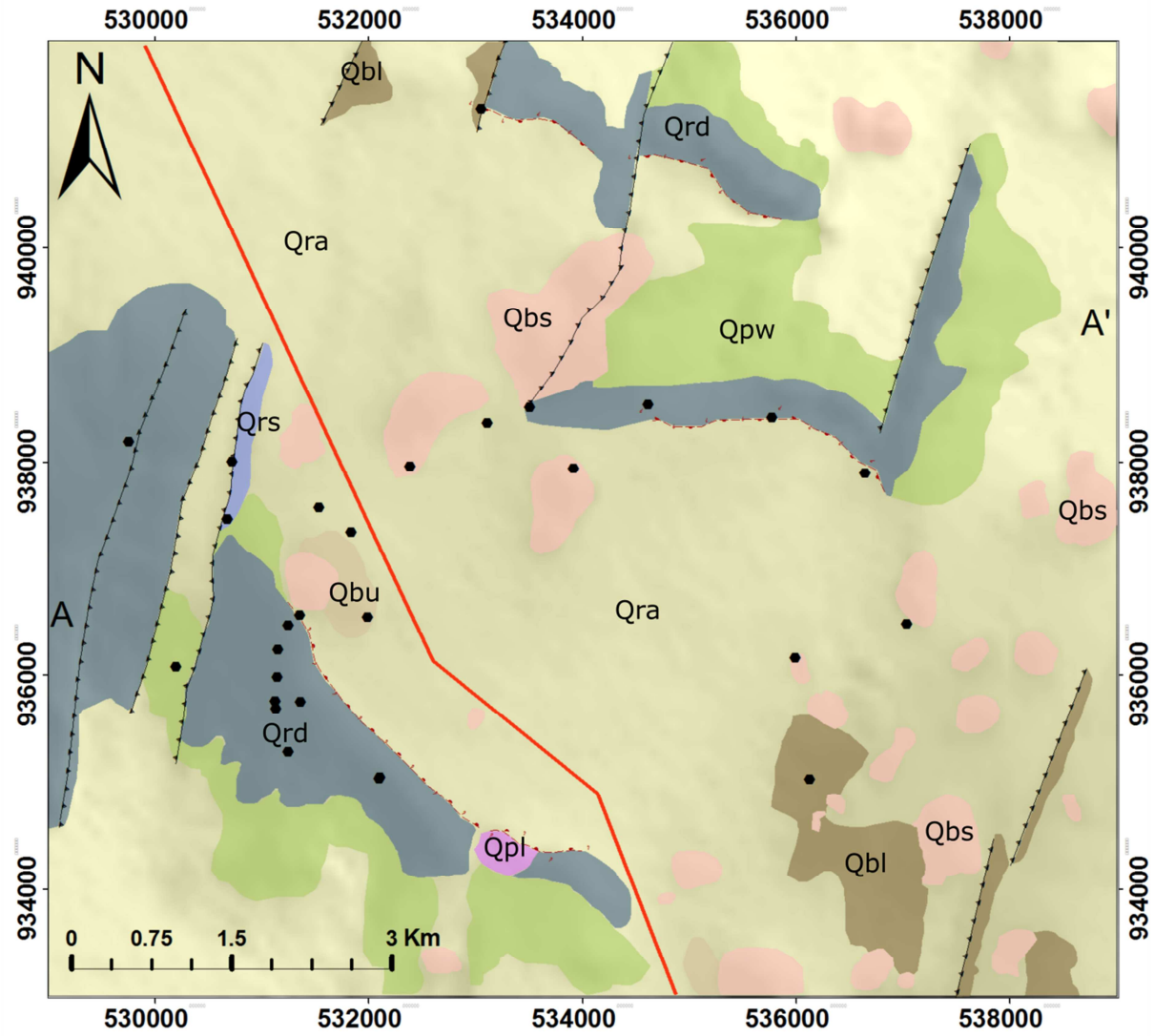

Legend

Symbols

- Geochemical sample points
- NNE-SSW trending normal fault
- Ring-normal fault
- Road

Lithology

- Upper Basaltic Lava Flow (Qbu)
- Basaltic scoria (Qbs)
- Ash flow (Qra)
- Lower Basaltic Lava Flow (Qbl)
- Rhyolitic Lava Dome (Qrd)
- Ash and Pumice Fall (Qpl)
- Pumice Flow (Qpw)
- Rhyolitic Lava Flow (Qrf)

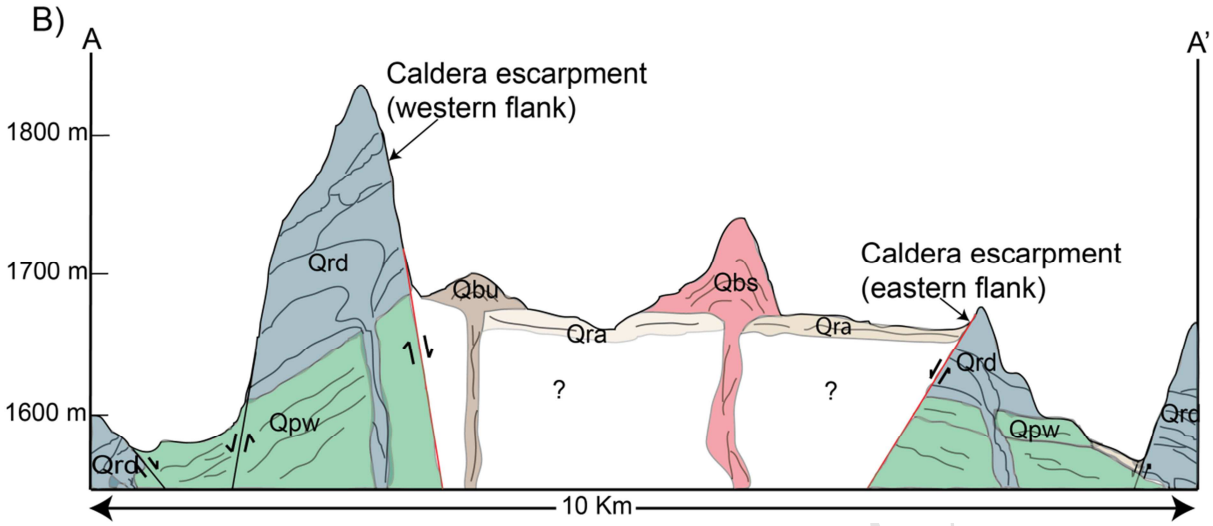

C)

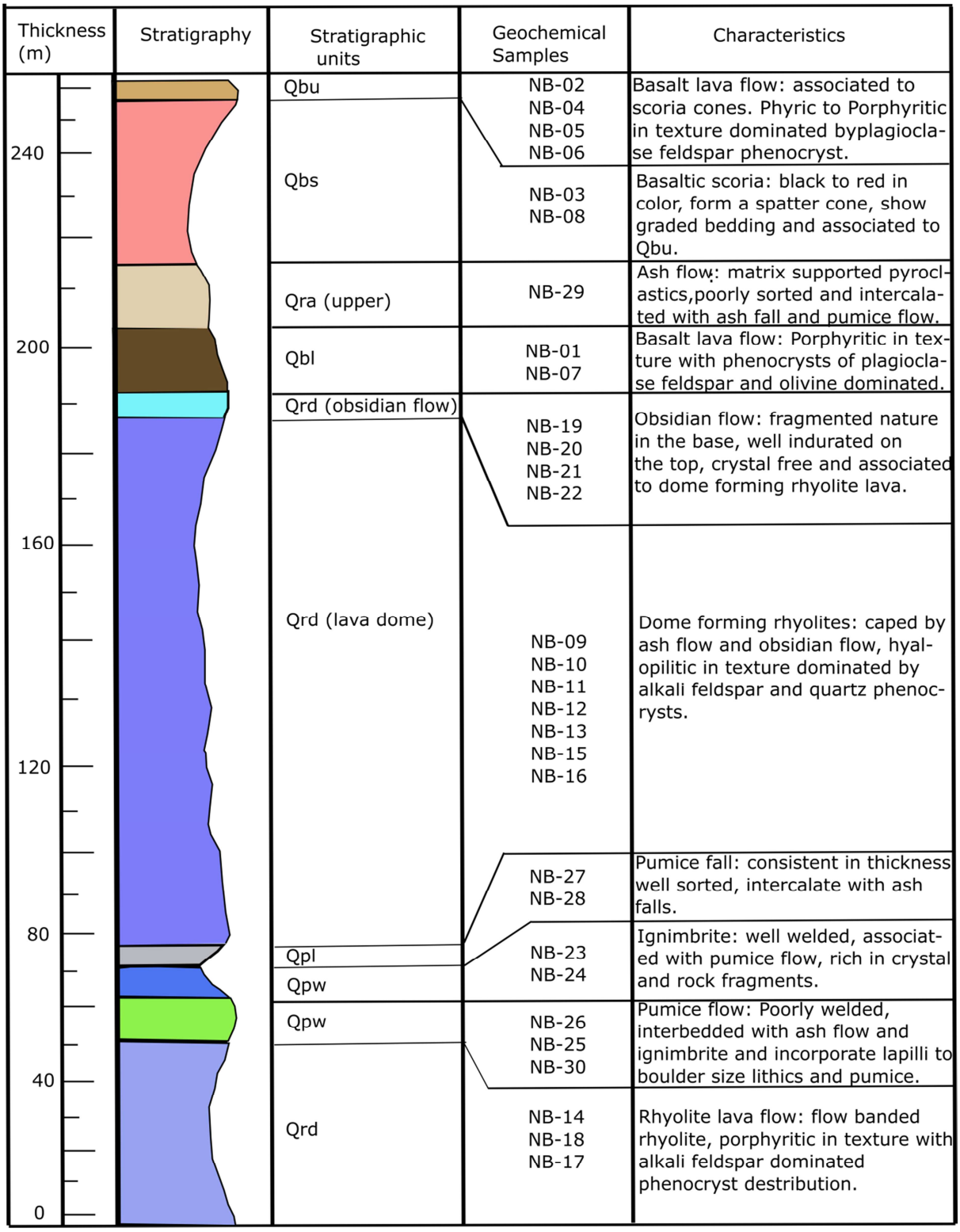
Thickness (m)
Stratigraphy
Stratigraphic units
Geochemical Samples
Characteristics
240
200
160
120
80
40
0
Qbu
Qbs
Qra (upper)
Qbl
Qrd (obsidian flow)
Qrd (lava dome)
Qpl
Qpw
Qpw
Qrd
NB-02 NB-04 NB-05 NB-06
Basalt lava flow: associated to scoria cones. Phyric to Porphyritic in texture dominated byplagioclase feldspar phenocryst.
NB-03 NB-08
Basaltic scoria: black to red in color, form a spatter cone, show graded bedding and associated to Qbu.
NB-29
Ash flow: matrix supported pyroclastics,poorly sorted and intercalated with ash fall and pumice flow.
NB-01 NB-07
Basalt lava flow: Porphyritic in texture with phenocrysts of plagioclase feldspar and olivine dominated.
NB-19 NB-20 NB-21 NB-22
Obsidian flow: fragmented nature in the base, well indurated on the top, crystal free and associated to dome forming rhyolite lava.
NB-09 NB-10 NB-11 NB-12 NB-13 NB-15 NB-16
Dome forming rhyolites: caped by ash flow and obsidian flow, hyalopilitic in texture dominated by alkali feldspar and quartz phenocrysts.
NB-27 NB-28
Pumice fall: consistent in thickness well sorted, intercalate with ash falls.
NB-23 NB-24
Ignimbrite: well welded, associated with pumice flow, rich in crystal and rock fragments.
NB-26 NB-25 NB-30
Pumice flow: Poorly welded, interbedded with ash flow and ignimbrite and incorporate lapilli to boulder size lithics and pumice.
NB-14 NB-18 NB-17
Rhyolite lava flow: flow banded rhyolite, porphyritic in texture with alkali feldspar dominated phenocryst destribution.

Fig. 3

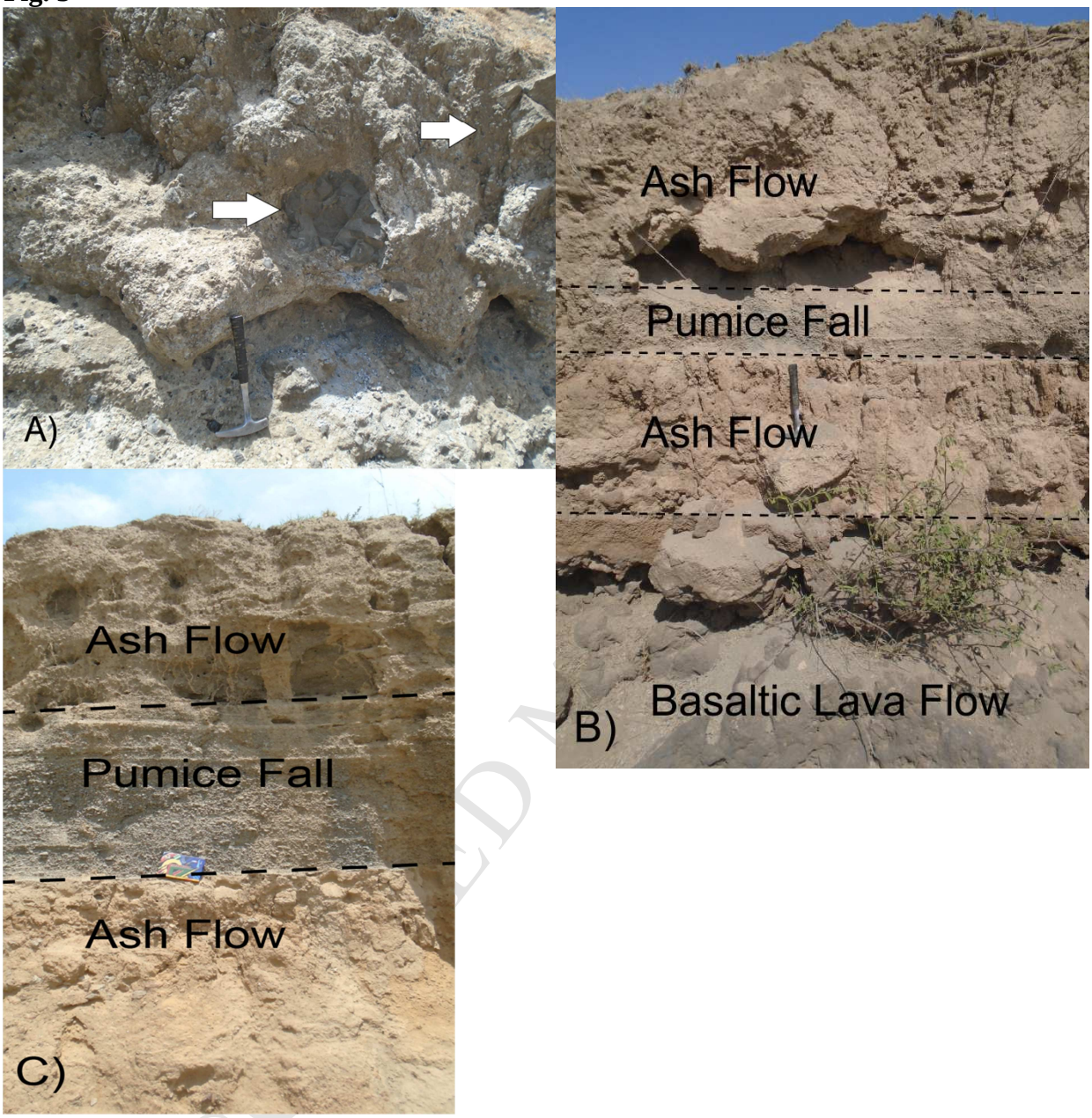
A)
Ash Flow
Pumice Fall
Ash Flow
B)
Basaltic Lava Flow
Ash Flow
Pumice Fall
Ash Flow
C)

Fig. 4

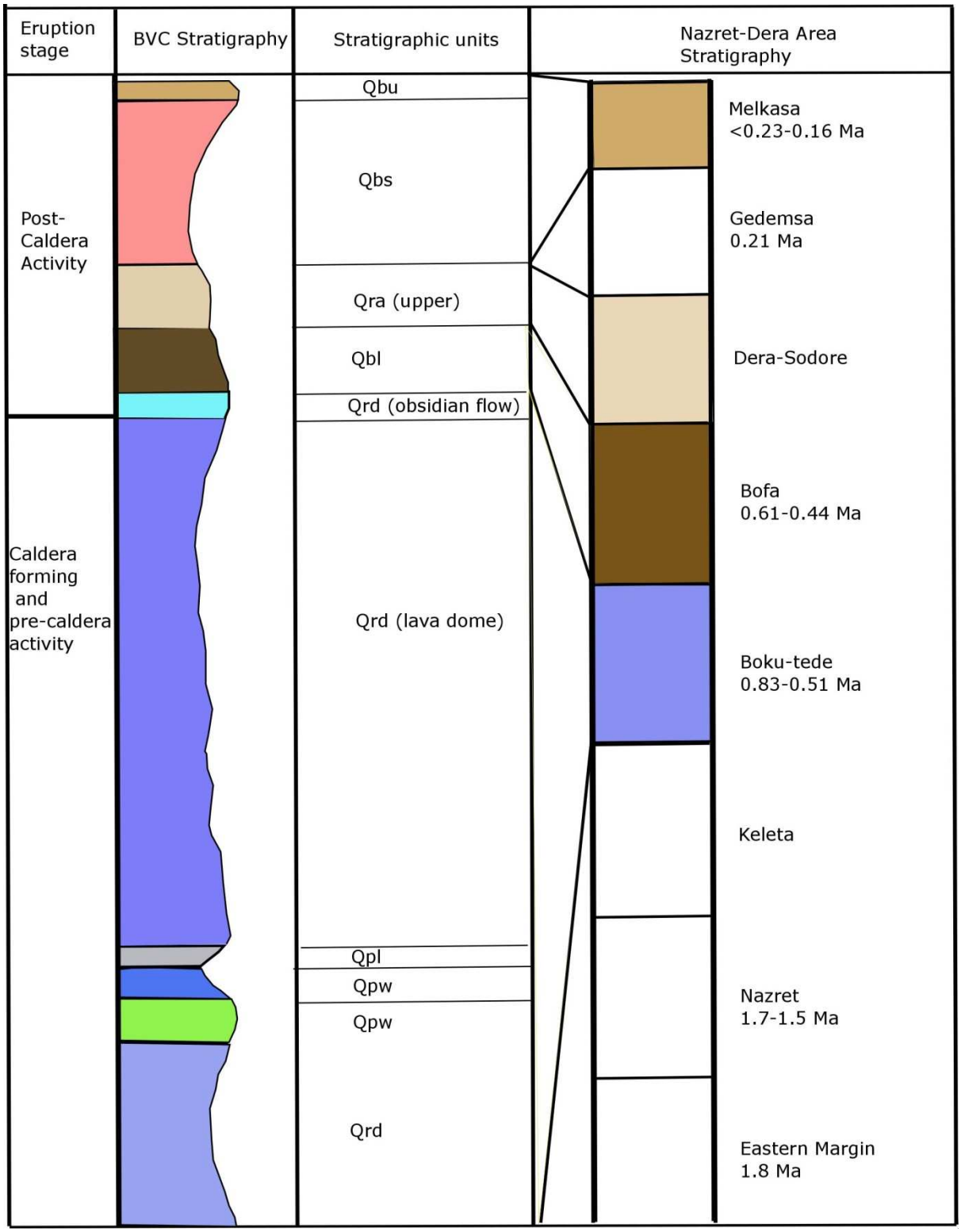
Eruption stage
BVC Stratigraphy
Stratigraphic units
Nazret-Dera Area Stratigraphy
Post-Caldera Activity
Caldera forming and pre-caldera activity
Qbu
Qbs
Qra (upper)
Qbl
Qrd (obsidian flow)
Qrd (lava dome)
Qpl
Qpw
Qpw
Qrd
Melkasa <0.23-0.16 Ma
Gedemsa 0.21 Ma
Dera-Sodore
Bofa 0.61-0.44 Ma
Boku-tede 0.83-0.51 Ma
Keleta
Nazret 1.7-1.5 Ma
Eastern Margin 1.8 Ma

Fig. 5

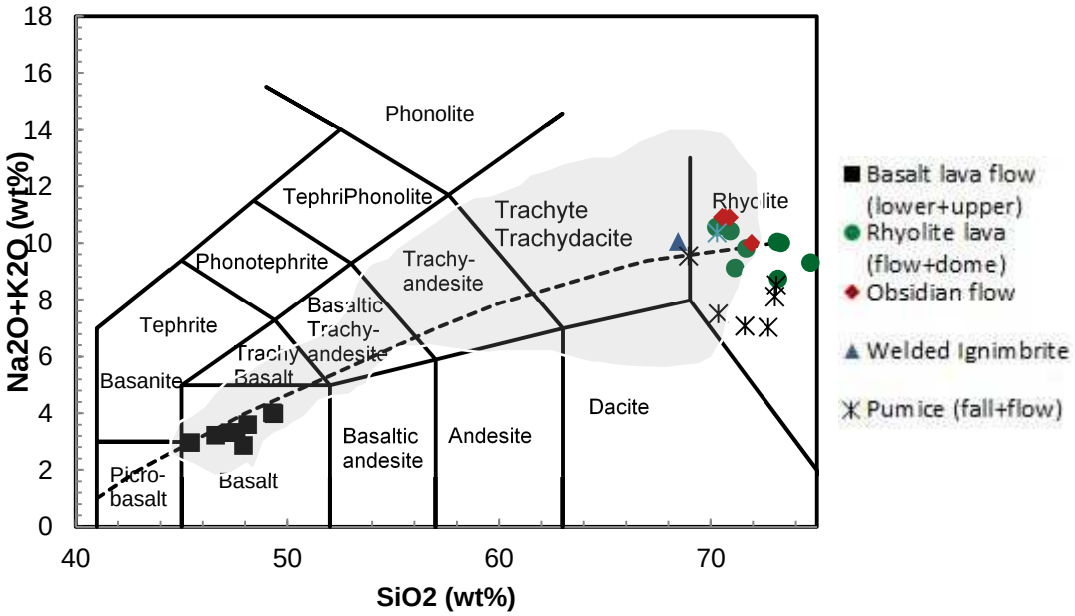

Fig.6

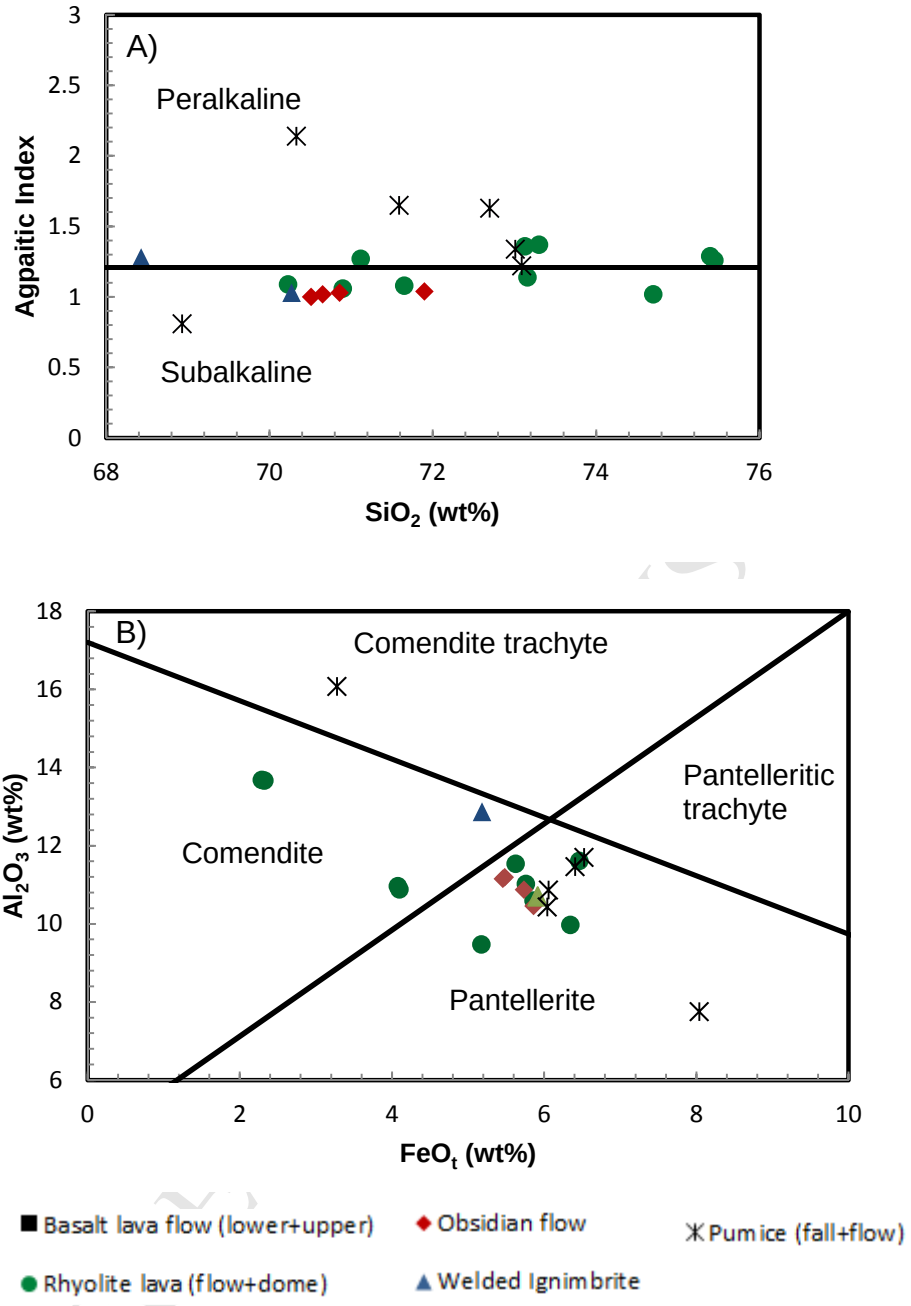
A)
Peralkaline
Subalkaline
Agpaitic Index
SiO2 (wt%)
B)
Comendite trachyte
Pantelleritic trachyte
Comendite
Pantellerite
Al2O3 (wt%)
FeOt (wt%)
Basalt lava flow (lower+upper)
Obsidian flow
Pumice (fall+flow)
Rhyolite lava (flow+dome)
Welded Ignimbrite

Fig.7

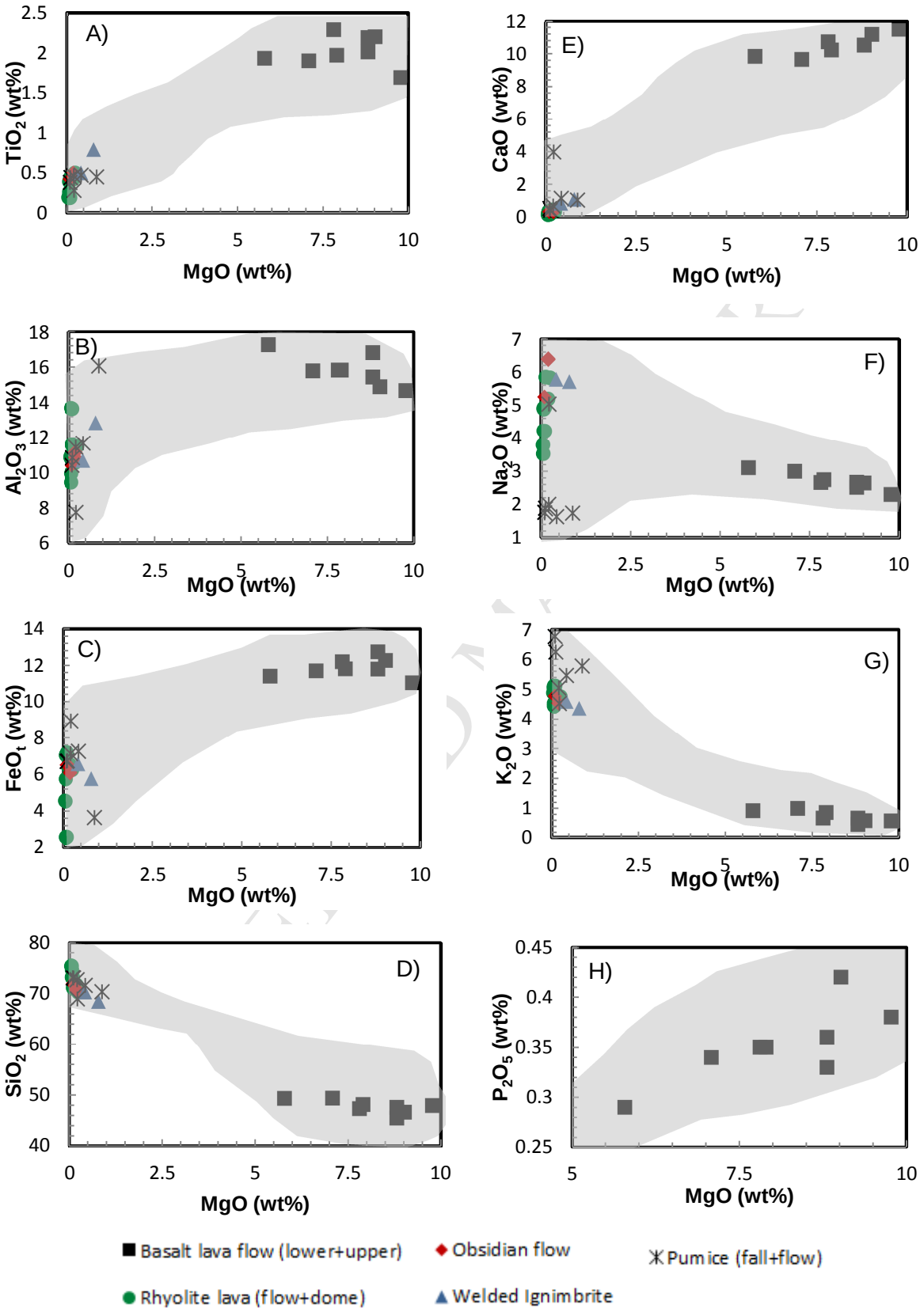
A)
TiO_2 (wt%)
MgO (wt%)
E)
CaO (wt%)
MgO (wt%)
B)
Al_2O_3 (wt%)
MgO (wt%)
F)
Na_2O (wt%)
MgO (wt%)
C)
FeO_t (wt%)
MgO (wt%)
G)
K_2O (wt%)
MgO (wt%)
D)
SiO_2 (wt%)
MgO (wt%)
H)
P_2O_5 (wt%)
MgO (wt%)
Basalt lava flow (lower+upper)
Obsidian flow
Pumice (fall+flow)
Rhyolite lava (flow+dome)
Welded Ignimbrite

Fig. 8

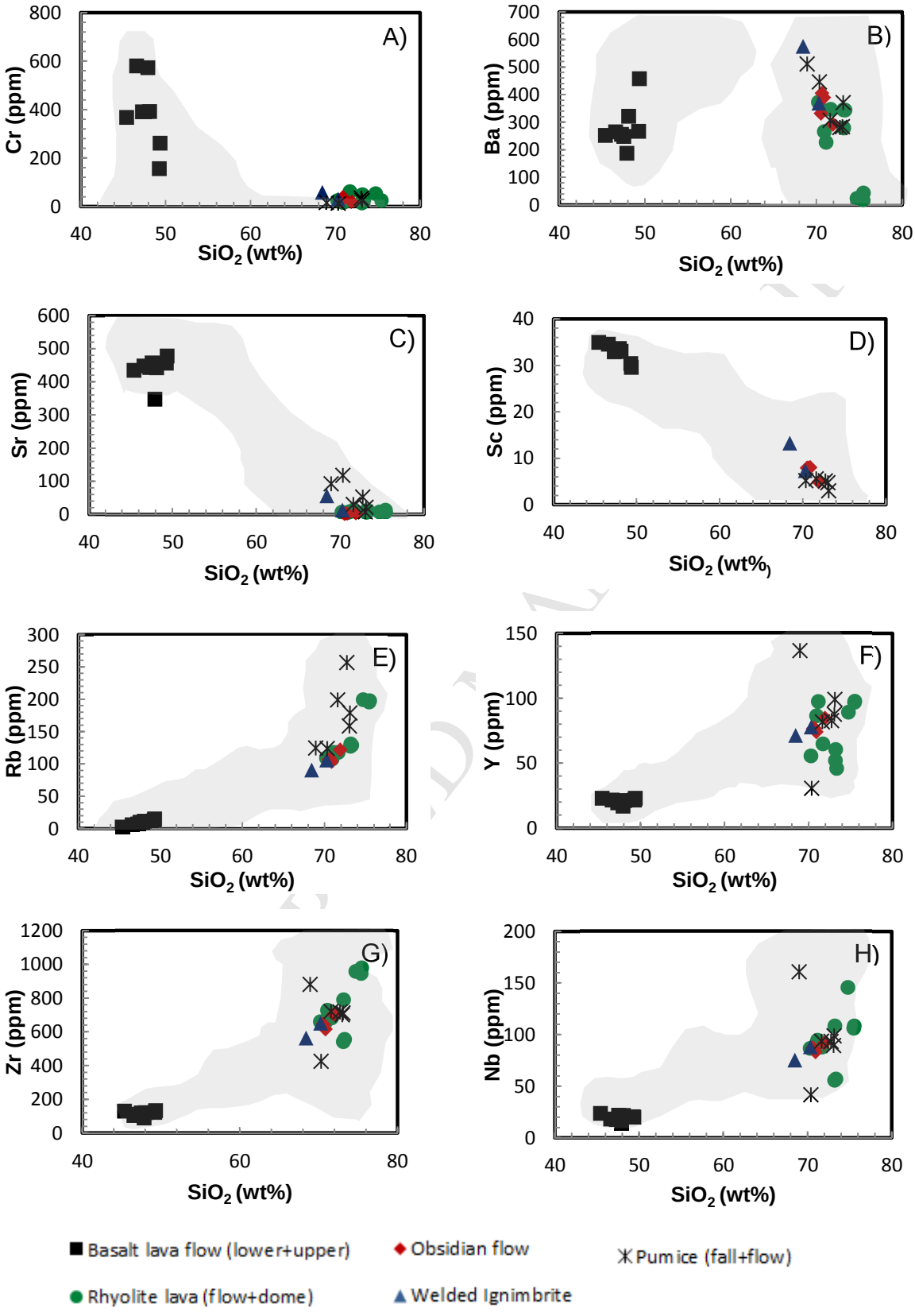
A)
Cr (ppm)
SiO2 (wt%)
B)
Ba (ppm)
SiO2 (wt%)
C)
Sr (ppm)
SiO2 (wt%)
D)
Sc (ppm)
SiO2 (wt%)
E)
Rb (ppm)
SiO2 (wt%)
F)
Y (ppm)
SiO2 (wt%)
G)
Zr (ppm)
SiO2 (wt%)
H)
Nb (ppm)
SiO2 (wt%)
Basalt lava flow (lower+upper)
Obsidian flow
Pumice (fall+flow)
Rhyolite lava (flow+dome)
Welded Ignimbrite

Fig. 9

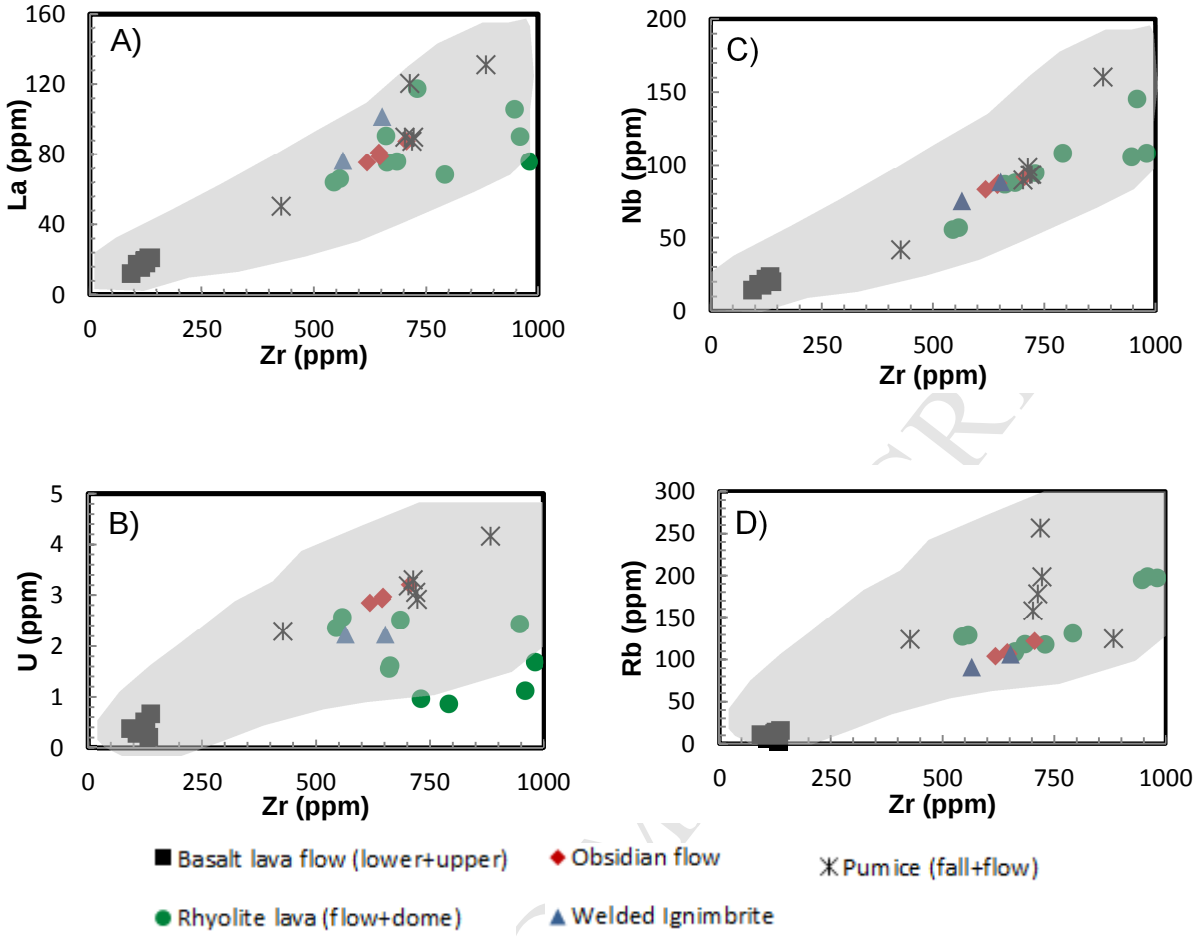

Fig. 10

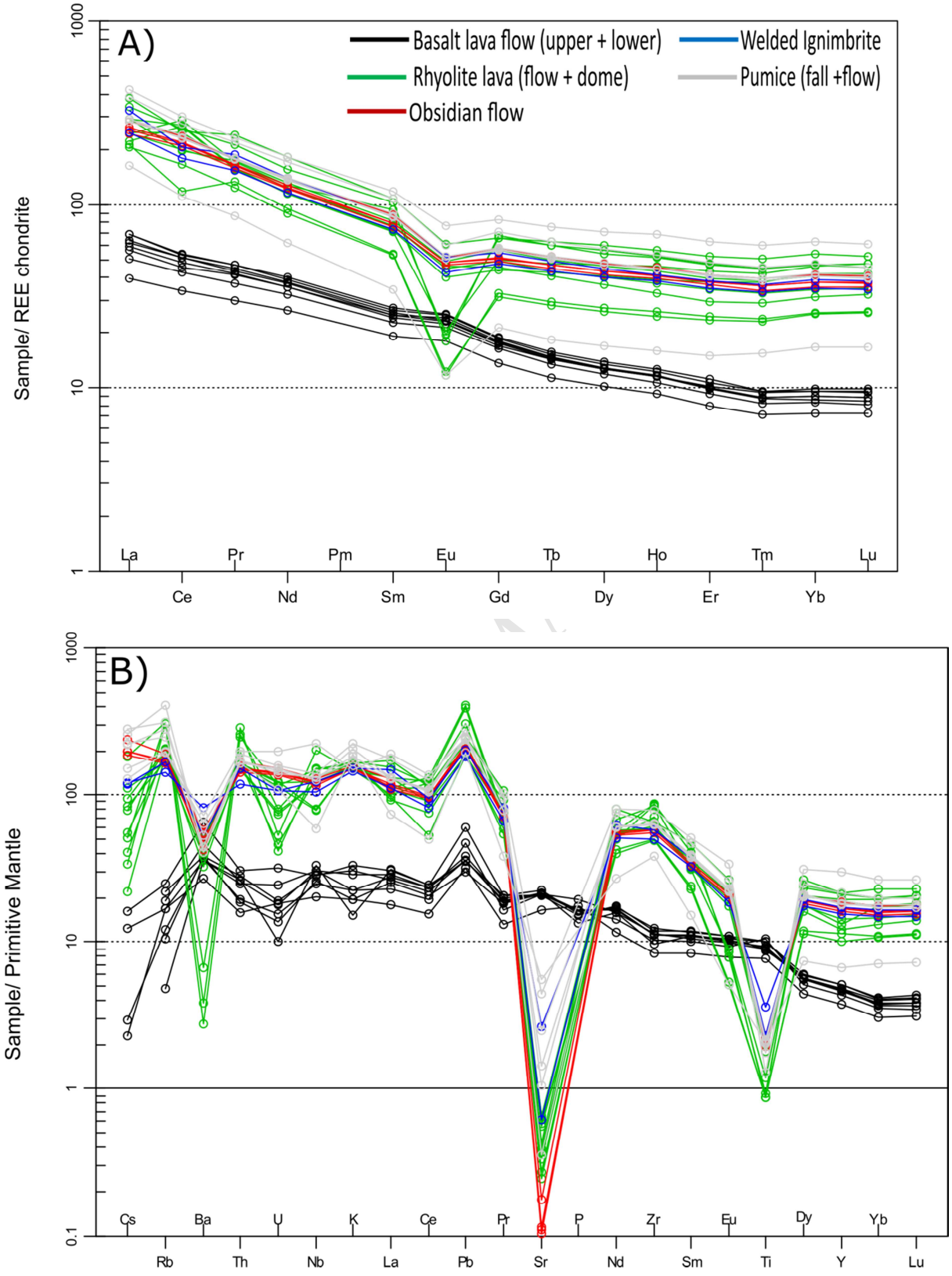
A)
Basalt lava flow (upper + lower)
Welded Ignimbrite
Rhyolite lava (flow + dome)
Pumice (fall +flow)
Obsidian flow
Sample/ REE chondrite
1000
100
10
1
La
Ce
Pr
Nd
Pm
Sm
Eu
Gd
Tb
Dy
Ho
Er
Tm
Yb
Lu
B)
Sample/ Primitive Mantle
1000
100
10
1
0.1
Cs
Rb
Ba
Th
U
Nb
K
La
Ce
Pb
Pr
Sr
P
Nd
Zr
Sm
Eu
Ti
Dy
Y
Yb
Lu

Fig. 11

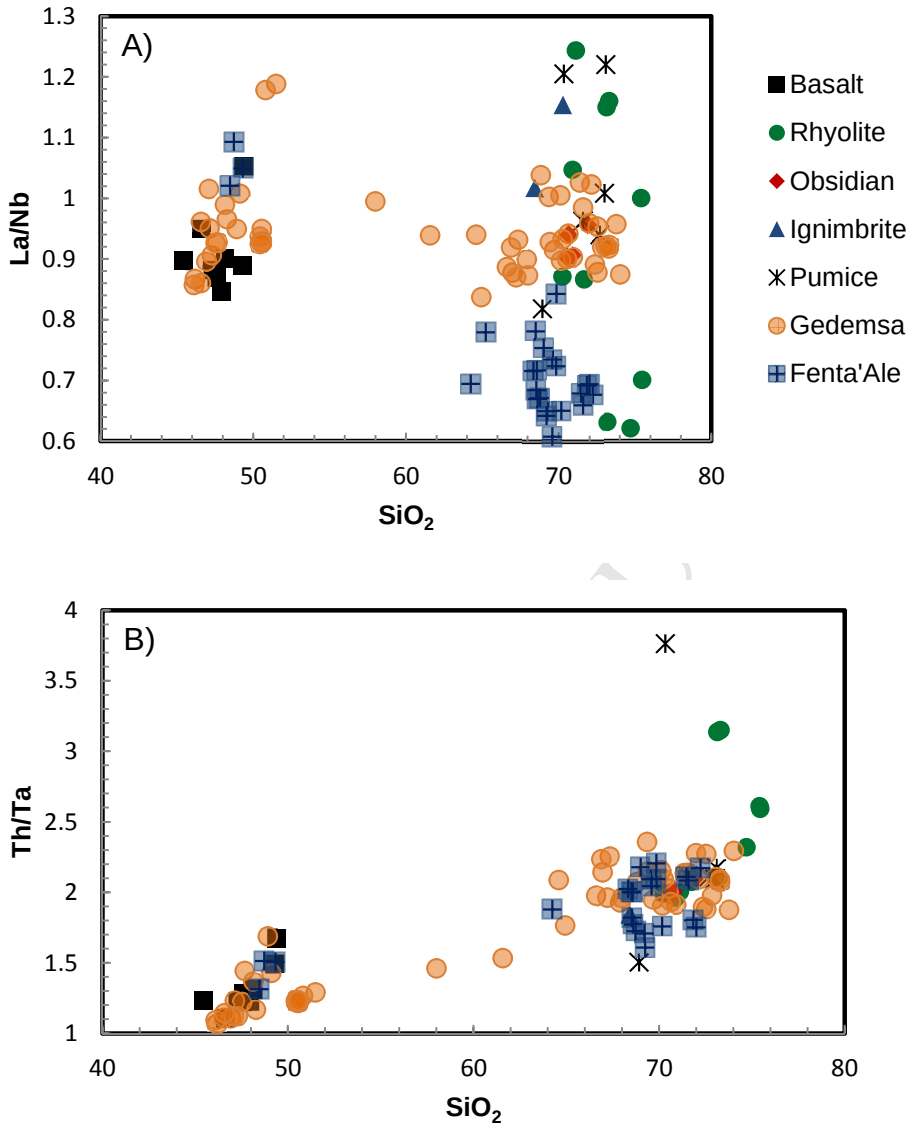
A)
La/Nb
SiO2
1.3
1.2
1.1
1
0.9
0.8
0.7
0.6
40
50
60
70
80
Basalt
Rhyolite
Obsidian
Ignimbrite
Pumice
Gedemsa
Fenta'Ale
B)
Th/Ta
SiO2
4
3.5
3
2.5
2
1.5
1
40
50
60
70
80

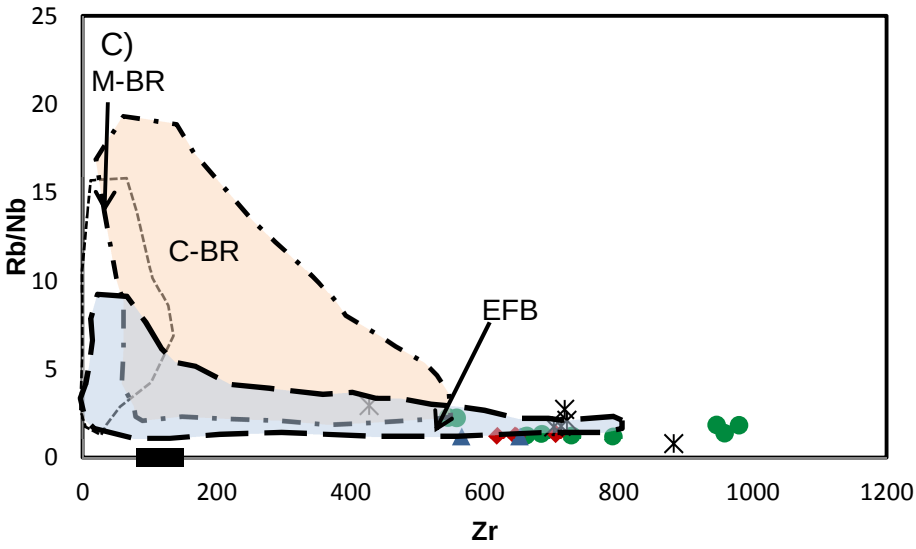
C)
M-BR
C-BR
EFB
Rb/Nb
Zr
0
5
10
15
20
25
0
200
400
600
800
1000
1200

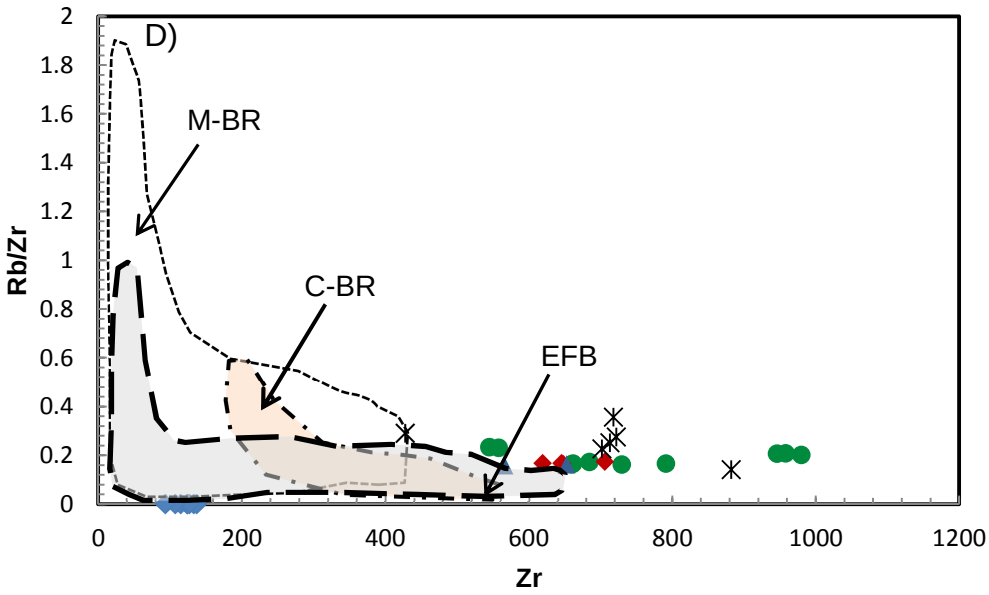
D)
M-BR
C-BR
EFB
Rb/Zr
Zr
0
0.2
0.4
0.6
0.8
1
1.2
1.4
1.6
1.8
2
0
200
400
600
800
1000
1200

Fig. 12

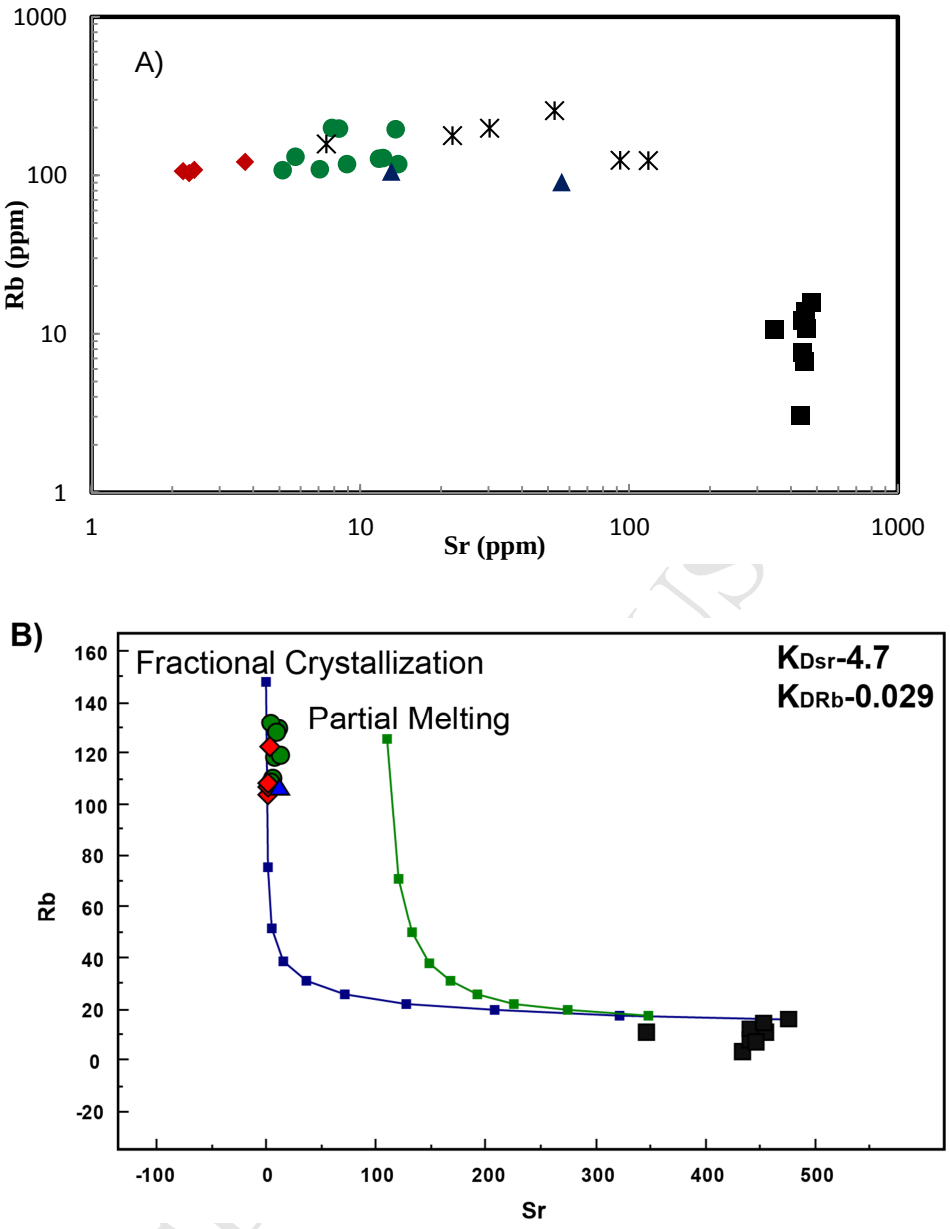
A)
1000
100
10
1
Rb (ppm)
1
10
100
1000
Sr (ppm)
B)
Fractional Crystallization
Partial Melting
KDsr-4.7
KDRb-0.029
160
140
120
100
80
60
40
20
0
-20
Rb
-100
0
100
200
300
400
500
Sr

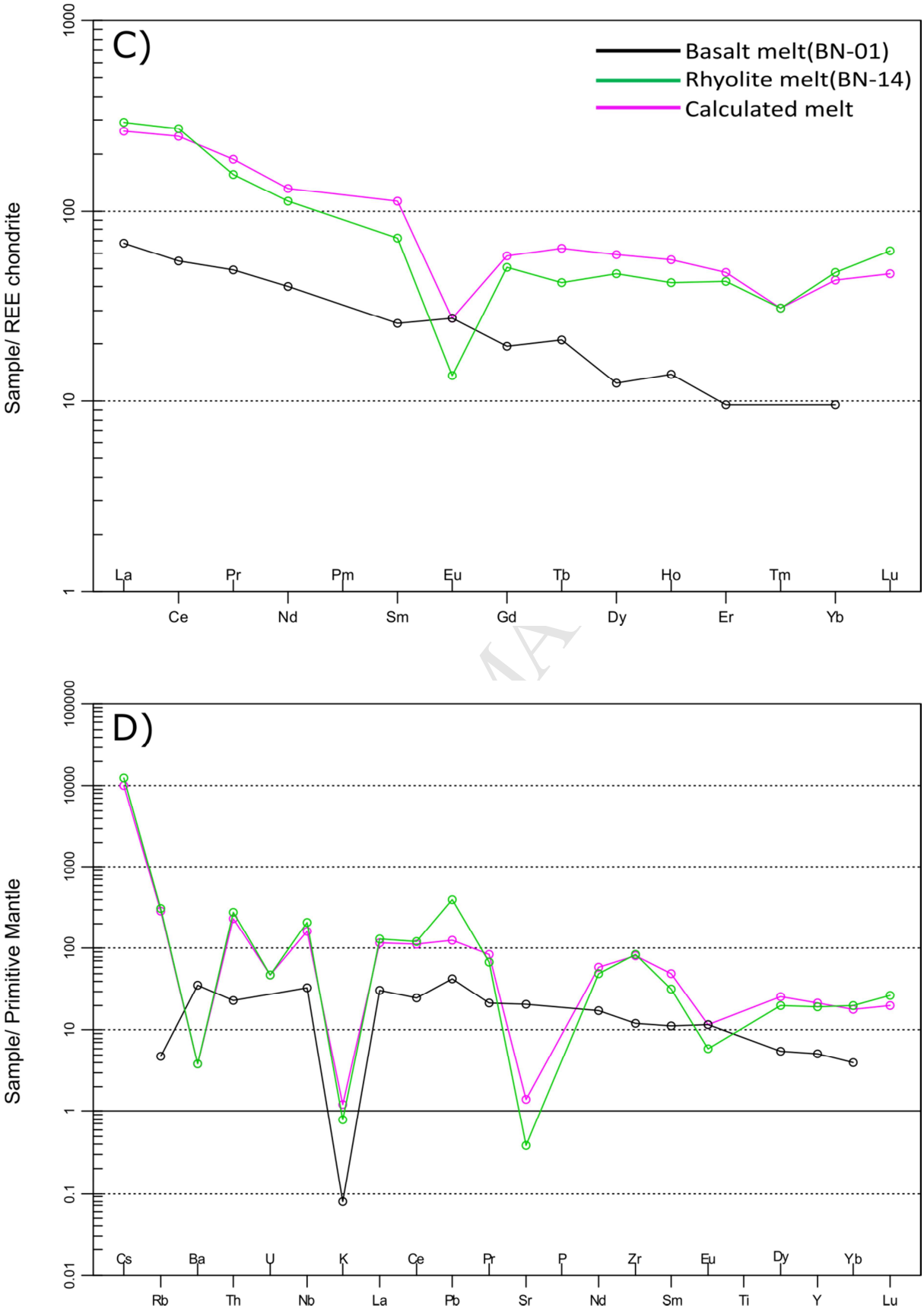
C)
Basalt melt(BN-01)
Rhyolite melt(BN-14)
Calculated melt
Sample/ REE chondrite
1000
100
10
1
La
Ce
Pr
Nd
Pm
Sm
Eu
Gd
Tb
Dy
Ho
Er
Tm
Yb
Lu
D)
Sample/ Primitive Mantle
100000
10000
1000
100
10
1
0.1
0.01
Cs
Rb
Ba
Th
U
Nb
K
La
Ce
Pb
Pr
Sr
P
Nd
Zr
Sm
Eu
Ti
Dy
Y
Yb
Lu

Fig. 13

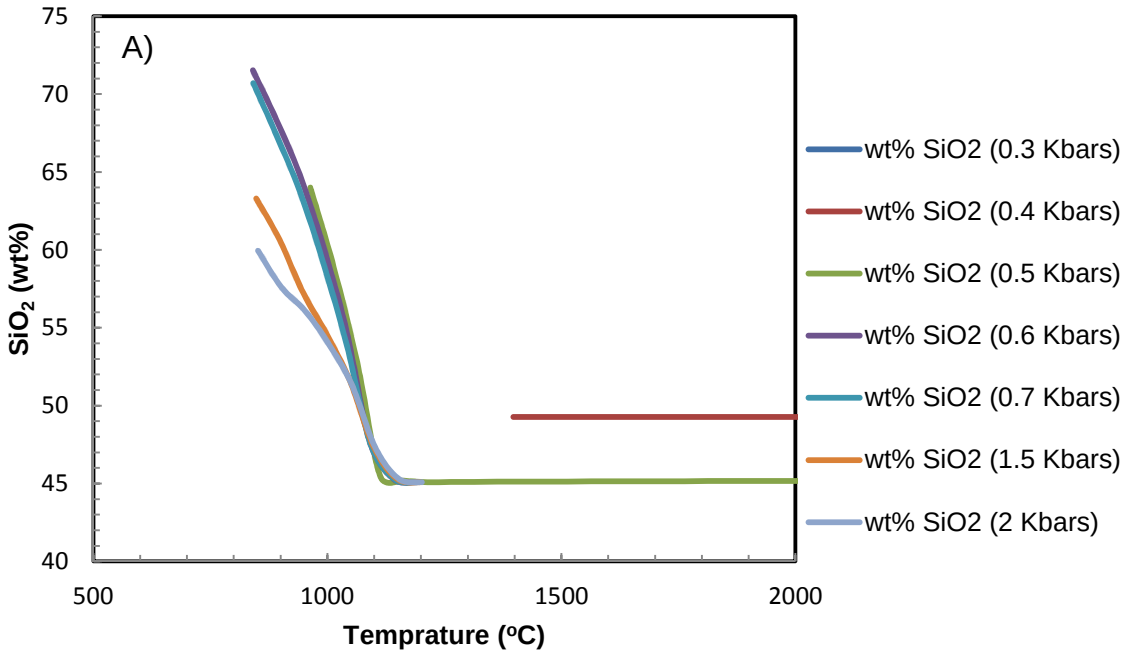
A)
75
70
65
60
55
50
45
40
500
1000
1500
2000
SiO2 (wt%)
Temprature (°C)
wt% SiO2 (0.3 Kbars)
wt% SiO2 (0.4 Kbars)
wt% SiO2 (0.5 Kbars)
wt% SiO2 (0.6 Kbars)
wt% SiO2 (0.7 Kbars)
wt% SiO2 (1.5 Kbars)
wt% SiO2 (2 Kbars)

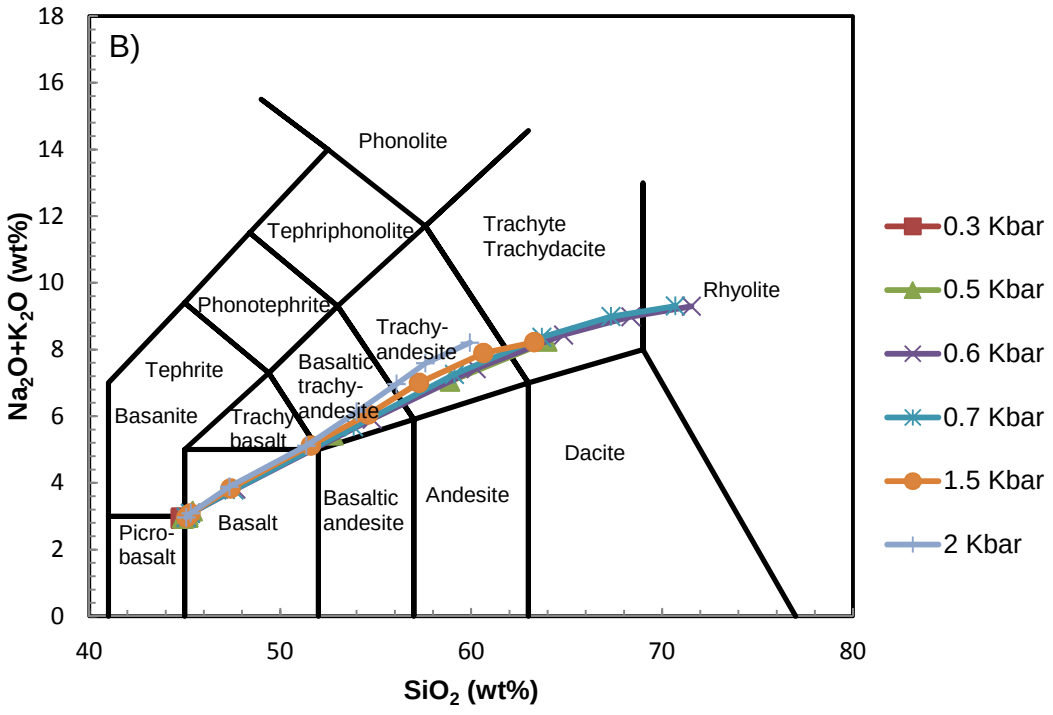
B)
18
16
14
12
10
8
6
4
2
0
40
50
60
70
80
Na2O+K2O (wt%)
SiO2 (wt%)
Phonolite
Tephriphonolite
Trachyte
Trachydacite
Rhyolite
Phonotephrite
Trachy-
andesite
Tephrite
Basaltic
trachy-
andesite
Basanite
Trachy
basalt
Dacite
Basaltic
andesite
Andesite
Basalt
Picro-
basalt
0.3 Kbar
0.5 Kbar
0.6 Kbar
0.7 Kbar
1.5 Kbar
2 Kbar

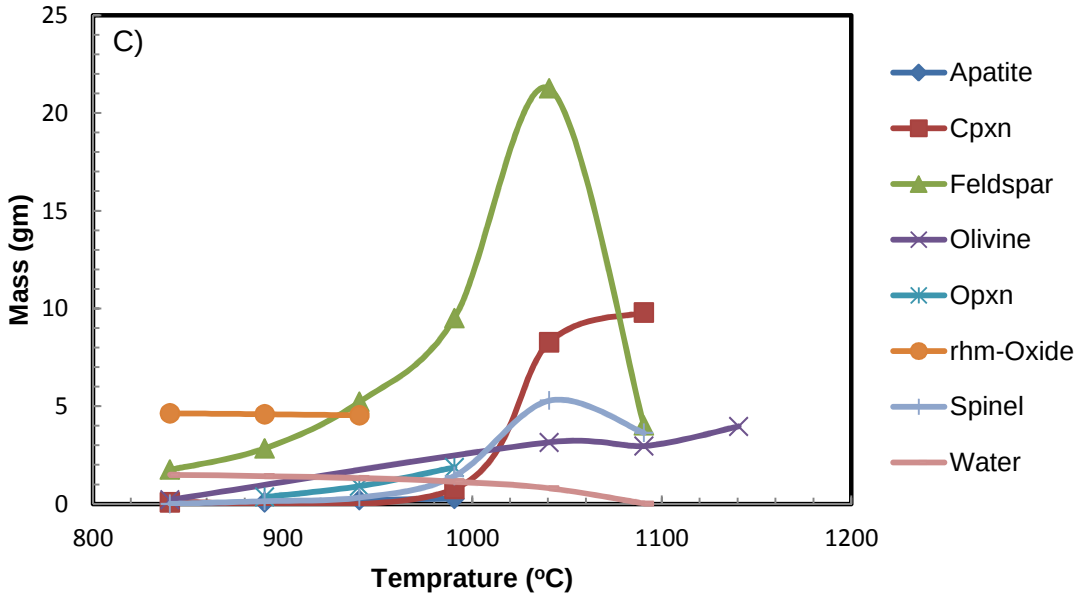
C)
25
20
15
10
5
0
Mass (gm)
800
900
1000
1100
1200
Temprature (ºC)
Apatite
Cpxn
Feldspar
Olivine
Opxn
rhm-Oxide
Spinel
Water

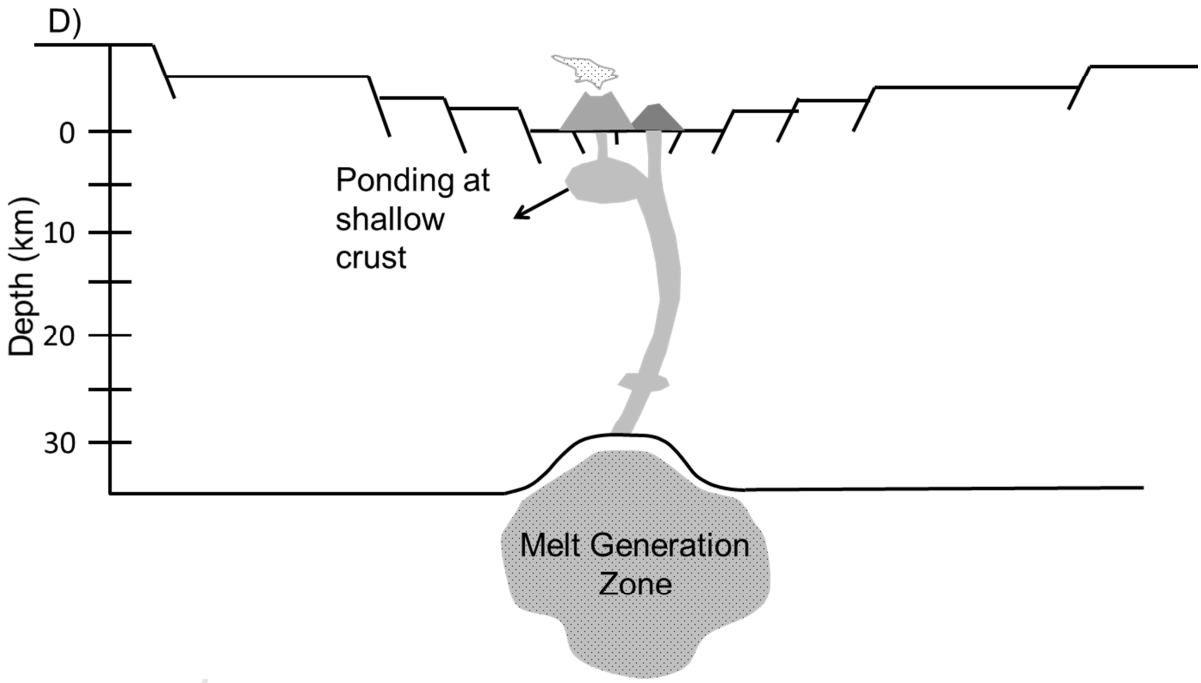
D)
0
10
20
30
Depth (km)
Ponding at
shallow
crust
Melt Generation
Zone

Highlight

- Boku volcanic complex is a Quaternary silicic center found at the axial zone of Main Ethiopian Rift which is composed of volcanic products sourced from two main episodes of volcanic activity; Boku pre-caldera/caldera forming and post caldera eruptive activity.
- The chemical compositions are bimodal; mainly basaltic and silicic with a lack of intermediate composition. The basalts are transitional to weakly subalkaline and the silicic rocks are dominantly peralkaline rhyolite.
- The geochemistry result imply the two groups of the rock, basaltic and peralkaline rhyolite, has the same source and linked by a fractional crystallization process with minor crustal contamination